East European Journal of Physics. **1.** 125-129 (2023)
DOI:10.26565/2312-4334-2023-1-15 ISSN 2312-4334

EFFECT OF COMPETING IONS ON MULTISORPTION (Cs^+, Sr^{2+}) BY COMPOSITE SORBENTS BASED ON NATURAL AND SYNTHETIC ZEOLITES†

Oleksii Yu. Lonin[a]*, Volodymyr V. Levenets[a], Oleksandr P. Omelnyk[a], Andriy O. Shchur[a]
[a]National Science Center "Kharkiv Institute of Physics & Technology"
1, Akademichna St., Kharkiv, 61108, Ukraine
**Corresponding Author e-mail: a_lonin@kipt.kharkov.ua; a_lonin@ukr.net*
Received December 26, 2022; revised January 20, 2023; accepted January 23, 2023

In the course of the research, the effect of competing ions (Na^{+}) on multisorption (Cs^+, Sr^{2+}) by composite sorbents based on natural and synthetic zeolites under static conditions was studied. It was found that the maximum concentration of competing ions (0.4 g of NaCl per 100 ml of solution) leads to a decrease in cesium sorption by 20%, and strontium sorption decreases by 10%. At the same time, high rates of sorption of cesium and strontium are preserved. Thus, for a composite sorbent (clinoptilolite -30%: zeolite NaX - 70%), the sorption of cesium was 67.9%, and the sorption of strontium was 87.6%. The analytical technique was developed on the basis of the PIXE (Proton Induced X-ray Emission) method and made it possible to qualitatively and quantitatively determine the content of isotopes. The work was performed at the analytical nuclear-physical complex "Sokil". The energy range of the electrostatic accelerator is 200-2000 keV. The complex made it possible to carry out all the main methods of analysis using ion beams. The targets were placed in the exit, at the Chamber for PIXE. To carry out measurements, a vacuum with a pressure of 10^{-4} Pa was created in the chamber. To excite the atoms of cesium, strontium, a proton beam with an energy of Ep≈1400 keV was used. The characteristic X-ray radiation of the L-series of cesium atoms and K-series of strontium atoms was recorded by two detectors: XR-100CR Si-PIN X-Ray and Ge(HP). The sorption coefficient (Sorption, %) was used as a quantitative characteristic of the interaction of sorbents with cesium, strontium.
Keywords: *cesium; strontium; liquid radioactive waste; zeolites; static sorption*
PACS: 68.43.Mn; 82.50.-m

One of the main problems in the further development of nuclear energy is the management of radioactive waste. Radioactive waste is divided by activity (high activity, medium activity, low activity), by physical state (solid, liquid and gaseous). A significant part of radioactive waste is liquid radioactive waste. Thus, in 2020, 8783 m^3 of liquid radioactive waste was accumulated at Ukrainian NPPs [1,2]. For the purification and subsequent processing of liquid radioactive waste, thermal, sorption, and membrane methods are used, and they also include filtration, coprecipitation and coagulation of sediments and suspensions, ion exchange, osmosis and reverse osmosis, electrodialysis, and evaporation of solutions [3–8]. The most promising is the sorption method, which includes various directions of sorption. When choosing a sorbent for purification of liquid radioactive sorbents, the following factors are taken into account: sorption efficiency, structural stability (radiation resistance, chemical resistance, and thermal stability), cost, and production conditions [9].

Numerous studies have shown the effectiveness of natural ion-exchange sorbents in experiments. This group includes bentonite, vermiculite and clinoptilolite. When using them, it must be taken into account that natural sorbents are characterized by a narrow spectrum of sorbed radionuclides. The most effective use of clinoptilolite is for sorption of cesium. In this case, it should be taken into account that, depending on the deposit and the depth of occurrence, the composition of the exchange ions of the zeolite and the content of crystalline water may change. A change in these factors can have a significant effect on the sorption properties of the zeolite.

Synthetic zeolites are distinguished by a stable composition of exchange ions, which is set during the synthesis process. As well as a more developed structure with a large number of exchange centers. This is due to the predominance of Al ions in the structure of synthetic zeolites. Al ions are the basis for the formation of an excess negative charge. The negative charge is formed due to the interaction with the fourth O atom, which is included in the tetrahedral structure of the zeolite [10-12].

Therefore, the most promising is the use of composite sorbents, which include a natural component and a synthetic component in their composition. Such a composition significantly expands the list of sorbed radionuclides. The most promising is the composition based on natural zeolite (clinoptilolite) and synthetic zeolite.

When conducting model experiments on the sorption of radionuclides from liquid radioactive waste, the following factors must be taken into account: a complex radionuclide composition and the presence of competing ions.

In the work published earlier, the processes of multisorption on clinoptilolite and composite sorbent based on zeolites were considered, but the effect of competing ions on sorption processes was not considered in this work [13].

The issues of studying of sorption Cs^+ and Sr^{2+} are very relevant and are reflected in modern publications [14-18].

Therefore, in this work, multisorption (Cs^+, Sr^{2+}) by sorbents in the presence of an increasing content of competing ions (Na^+) was considered.

† ***Cite as:*** O.Yu. Lonin, V.V. Levenets, O.P. Omelnyk, and A.O. Shchur, East Eur. J. Phys. **1**, 125 (2023), https://doi.org/10.26565/2312-4334-2023-1-15

MATERIALS AND METHODS

Research objects

Nitric acid salts $CsNO_3$ and $Sr(NO_3)_2$ served as sources of cesium and strontium ions. 100 ml of a solution containing Cs^+ ions (0.02 g $CsNO_3$ per 100 mL solution) and Sr^{2+} ions (0.02 g $Sr(NO_3)_2$ per 100 mL solution) was prepared. Taking into account the fact that the interaction of Sr^{2+} with CO_3^{2-} forms a poorly soluble compound, NaCl was used as a source of competing ions. This made it possible to consider the influence of sorption processes competing without harm. When considering the influence of competing ions, different concentrations of NaCl in the test solution were considered: 0.02 g of NaCl per 100 mL of solution; 0.04 g NaCl per 100 ml solution; 0.2 g NaCl per 100 mL solution; 0.4 g NaCl per 100 ml solution.

Natural zeolite (clinoptilolite) and synthetic NaX zeolite in the following compositions were used as the composite sorbents considered in the work:

1. clinoptilolite - 100% : zeolite NaX - 0%;
2. clinoptilolite - 50%: zeolite NaX - 50%;
3. clinoptilolite - 25%: zeolite NaX - 75%.

The choice of compositions 2 and 3 is due to the studies conducted earlier [19]. These studies made it possible to determine the optimal compositions based on natural and synthetic zeolites.

Sorption experiment (sorption)

Sorption was carried out under static conditions using sorbent fractions of 0.1 mm. The weight of the sorbent used in the experiment was 0.1 g. A weighed portion of the sorbent was placed in 20 mL of the test solution. Periodically, the solution with the sorbent was forcibly mixed.

The experiment lasted 24 hours with periodic sampling. Sorption equilibrium in the zeolite-cesium system occurs within 1 hour. The increase in the time of the experiment was carried out taking into account the time of onset of sorption equilibrium in the zeolite-strontium system, which occurs within 24 hours [20].

Targets preparation

The targets were prepared on a carbon substrate. The carbon substrate was prepared from carbon rods. The carbon substrate had a length of 10.00 mm and a thickness of 2.00 mm.

A solution in an amount of 0.05 mL containing a mixture of isotopes (cesium, strontium) was deposited on a carbon substrate and dried by heating to 35°C.

The targets prepared in this way were preserved after the initial use and could be subjected to further studies under the conditions given below [20-22].

ANALYTICAL PART OF THE EXPERIMENT

The analytical part of the work was performed on the analytical nuclear-physical complex "Sokol" [20-22]. The energy range of the electrostatic accelerator is 200-2000 keV. The complex made it possible to carry out all the main methods of analysis using ion beams. The complex made it possible to irradiate the objects under study with singly and doubly charged gas ions from hydrogen to xenon. The complex had 5 outputs, on which various nuclear physics techniques were implemented: an output for recording characteristic X-ray emission (the Chamber for PIXE (Proton Induced X-ray Emission)); the beam exit to atmosphere; the output for the determination of Rutherford backscattering (the Chamber RBS); the Nuclear Microbeam and the ion irradiation channel.

The targets were placed in the exit, at the Chamber for PIXE. To carry out measurements, a vacuum with a pressure of 10^{-4} Pa was created in the chamber. To excite the atoms of cesium, strontium, a proton beam with an energy of Ep≈1400 keV was used. This energy made it possible to excite the characteristic X-ray radiation of the L-series of cesium atoms and the K-series of strontium atoms. The characteristic X-ray radiation was measured using XR-100CR Si-PIN X-Ray detector with an energy distribution of 155 eV along the 6.4 keV line. The detector was placed at a distance of 7 cm from the target, at an angle of 135 ° to the proton beam, outside the window with beryllium foil 25 μm thick. XR-100CR Si-PIN X-Ray the detector was equipped with a Ø 1.5 mm collimator and a 56 μm thick mylar absorber [20-22]. The choice of the collimator and absorber took place taking into account the parameters of the detector when measuring the dead time and the intensity of the characteristic X-ray radiation.

The characteristic X-ray radiation of the K series of strontium atoms was recorded by two detectors: XR-100CR Si-PIN X-Ray and Ge(HP). The second detector was used to increase the detection efficiency of the K-series radiation of strontium atoms (14.164 keV).

Ge(HP) the detector was based on an ultrapure germanium crystal with a crystal thickness of 8.5 mm and a sensitive surface area of 25 mm^2. When working with a Ge (HP) detector, the SBS-75 pulse signal board was used as a spectrometric amplifier, a multichannel amplitude analyzer, and a spectrometric pulse accumulator.

RESULTS AND DISCUSSION

The sorption coefficient (Sorption, %) was used as a quantitative characteristic of the interaction of sorbents with cesium, strontium, and was calculated by the formula (1):

$$Sorption, \% = \frac{(C_0 - C_{eq}) \cdot 100\%}{C_0} \quad (1)$$

where C_o and C_{eq} are the initial and equilibrium concentration of the solution, mg/ml.

The obtained results are presented in Tables 1-3.

For clinoptilolite, the effect of competing ions in small amounts (0.02 g of NaCl per 100 ml of solution; 0.04 g of NaCl per 100 mL of solution) does not lead to a significant decrease in the sorption of cesium and strontium (Table.1). An increase in the content of competing ions (0.2 g NaCl per 100 mL of solution; 0.4 g NaCl per 100 mL of solution) leads to a decrease in the sorption of cesium and strontium by ~20%.

For composite sorbent № 2, an unusual effect of competing ions was observed. This is due to the introduction of NaX zeolite into the composition of the sorbent. At low concentrations of competing ions (0.02 g of NaCl per 100 mL of solution; 0.04 g of NaCl per 100 mL of solution), an increase in the sorption of cesium and strontium by 40% was observed during the first hour of sorption. However, by the time the sorption equilibrium was reached (24 hours), the change in sorption did not exceed 5% (Table 2).

Table 1. Sorption coefficients of cesium and strontium from a mixture of solution by clinoptilolite under static conditions in the presence of competing ions

Sorption time, h	Competing compound	The number of competing compounds per 100 mL of solution, g.	Cesium sorption coefficients, %	Strontium sorption coefficients, %
1	-	-	86.0	38.0
6	-	-	97.7	38.0
24	-	-	97.8	53.3
1	Sodium chloride	0.02	81.5	28.5
6	Sodium chloride	0.02	93.7	34.6
24	Sodium chloride	0.02	94.5	50.8
1	Sodium chloride	0.04	73.1	12.0
6	Sodium chloride	0.04	91.6	29.7
24	Sodium chloride	0.04	94.4	50.3
1	Sodium chloride	0.2	50.0	8.5
6	Sodium chloride	0.2	80.6	35.0
24	Sodium chloride	0.2	81.8	43.9
1	Sodium chloride	0.4	35.4	5.7
6	Sodium chloride	0.4	61.4	8.5
24	Sodium chloride	0.4	75.4	34.6

Table 2. Sorption coefficients of cesium and strontium from a mixture of solution by a composite sorbent 50/50 under static conditions in the presence of competing ions

Sorption time, h	Competing compound	The number of competing compounds per 100 mL of solution, g.	Cesium sorption coefficients, %	Strontium sorption coefficients, %
1	-	-	24.3	13.6
6	-	-	76.3	76.8
24	-	-	89.1	93.7
1	Sodium chloride	0.02	63.9	50.0
6	Sodium chloride	0.02	87.6	90.9
24	Sodium chloride	0.02	88.9	93.6
1	Sodium chloride	0.04	66.1	49.4
6	Sodium chloride	0.04	86.7	86.0
24	Sodium chloride	0.04	88.0	88.4
1	Sodium chloride	0.2	33.7	35.4
6	Sodium chloride	0.2	68.2	76.6
24	Sodium chloride	0.2	79.3	86.5
1	Sodium chloride	0.4	26.0	28.5
6	Sodium chloride	0.4	61.5	73.3
24	Sodium chloride	0.4	64.3	85.4

An increase in the content of competing ions (0.2 g NaCl per 100 mL of solution; 0.4 g NaCl per 100 mL of solution) leads to a decrease in cesium sorption by ~20%, while strontium sorption decreased by ~10%.

For composite sorbent № 3, an unusual effect of competing ions was also observed. This is due to the introduction of NaX zeolite into the composition of the sorbent. At low concentrations of competing ions (0.02 g of NaCl per 100 mL of solution; 0.04 g of NaCl per 100 mL of solution), an increase in the sorption of cesium and strontium by 30% - 35% was observed during the first hour of sorption. However, by the time the sorption equilibrium was reached (24 hours), the change in sorption did not exceed 2 - 3% (Table 3).

An increase in the content of competing ions (0.2 g NaCl per 100 mL of solution; 0.4 g NaCl per 100 mL of solution) leads to a decrease in cesium sorption by ~20%, while strontium sorption decreased by ~10%.

The results obtained indicate that the introduction of a high content of competing ions into the solution (0.4 g of NaCl per 100 mL of solution) leads to a decrease in the sorption of cesium by clinoptilolite and composite sorbents by 20%.

Table 3. Sorption coefficients of cesium and strontium from a mixture of solution by a composite sorbent 30/70 under static conditions in the presence of competing ions

Sorption time, h	Competing compound	The number of competing compounds per 100 mL of solution, gr.	Cesium sorption coefficients, %	Strontium sorption coefficients, %
1	-	-	27.8	27.1
6	-	-	81.2	94.7
24	-	-	87.3	95.8
1	Sodium chloride	0.02	55.2	66.9
6	Sodium chloride	0.02	84.7	98.1
24	Sodium chloride	0.02	85.5	98.1
1	Sodium chloride	0.04	59.3	63.9
6	Sodium chloride	0.04	83.6	95.4
24	Sodium chloride	0.04	84.6	97.8
1	Sodium chloride	0.2	31.4	45.6
6	Sodium chloride	0.2	52.9	82.6
24	Sodium chloride	0.2	69.5	89.6
1	Sodium chloride	0.4	27.5	35.3
6	Sodium chloride	0.4	48.2	61.8
24	Sodium chloride	0.4	67.9	87.6

The inclusion of synthetic zeolite in the composition of the composite sorbent significantly changes the situation of sorption of strontium in the presence of competing ions (0.4 g of NaCl per 100 mL of solution). Thus, for clinoptilolite, strontium sorption decreases by 20%, while for composite sorbents, the presence of competing ions (0.4 g NaCl per 100 mL of solution) leads to a decrease in strontium sorption by only 10%.

CONCLUSIONS

The results obtained indicate that during multisorption (cesium, strontium), clinoptilolite exhibits high sorption properties for cesium (Ks - 97.8%), and strontium sorption is only 53.3%.

At the same time, composite sorbents exhibit higher strontium sorption (Ks (50/50) - 93.4%, Ks (30/70) - 95.8%). And the sorption of cesium decreases slightly (Ks (50/50) - 89.1%, Ks (30/70) - 87.3%). This fact significantly expands the use of composite sorbents based on zeolites.

The concentration of competing ions in a solution significantly affects multisorption. At the maximum concentration of competing ions (0.4 g of NaCl per 100 ml of solution), cesium sorption decreases by 20%, and strontium sorption by 10%.

At the same time, high rates of sorption of cesium and strontium are preserved. So, for a composite sorbent (clinoptilolite - 50%: zeolite NaX - 50%), the sorption of cesium was 64.3%, and the sorption of strontium was 85.4%. For the composite sorbent (clinoptilolite - 30%: zeolite NaX - 70%), the cesium sorption was 67.9%, and the strontium sorption was 87.6%.

The results obtained confirm the effectiveness of using composite sorbents based on natural and synthetic zeolites for the purification of liquid radioactive waste.

ORCID IDs

Oleksii Yu. Lonin, https://orcid.org/0000-0002-5386-3825; **Volodymyr V. Levenets,** https://orcid.org/0000-0002-6439-0576
Oleksandr P. Omelnyk, https://orcid.org/0000-0003-2467-3632; **Andriy O. Shchur**, https://orcid.org/0000-0002-6619-4069

REFERENCES

[1] *Management of radioactive waste during the operation of the NPP of the SE*, "NAEK "Energoatom". https://www.energoatom.com.ua/uploads/others/RAO_2018.pdf, 2020 (accessed of 31 December 2020)
[2] State Nuclear Regulatory Inspectorate of Ukraine, *Report on the state of nuclear and radiation safety in UKRAINE in 2020.* https://snriu.gov.ua/storage/app/sites/1/uploaded-files/%D0%94%D0%BE%D0%BF%D0%BE%D0%B2%D1%96%D0%B4%D1%8C_%D0%AF%D0%A0%D0%91_2020_EN.pdf
[3] F.M. McEvoy, D.I. Schofield, R.P. Shaw, and S. Norris, Science of The Total Environment, **571**, 507 (2016). https://doi.org/10.1016/j.scitotenv.2016.07.018
[4] Uatom, Kyiv, Ukraine, Radwaste Management at Operating NPPs, https://www.uatom.org/en/radwaste-management-at-operating-npps
[5] R.O. Abdel Rahman, H.A. Ibrahium, and Yung-Tse Hung, Water, **3**(2), 551 (2011). https://doi.org/10.3390/w3020551
[6] M. Šljivić-Ivanović, and I. Smičiklas, "Advances in Construction and Demolition Waste Recycling", Woodhead Publishing Series in Civil and Structural Engineering, 475 (2020). https://doi.org/10.1016/B978-0-12-819055-5.00023-1
[7] L.A. Henry, and V. Douhovnikoff, Annual Review of Environment and Resources, **33,** 437 (2008). https://doi.org/10.1146/annurev.environ.33.051007.082437

[8] F. Šebesta, J. John, A Motl, V. Peka, and E. Vacková, JRNC, **220**(1), 65 (1997). https://doi.org/10.1007/BF02035349
[9] L.G. Gerasimova, D.V. Maiorov, M.V. Maslova, V.A. Matveev, and V.M. Shcherbakov, International scientific journal "Alternative energy and ecology", **2**(22), 39 (2005). https://cyberleninka.ru/article/n/razrabotka-tehnologii-polucheniya-i-primeneniya-sorbentov-radionuklidov-na-osnove-tehnogennyh-othodov-obogascheniya-apatito (in Russian)
[10] D. Breck, *Zeolite molecular sieves*, (Wiley, New York, 1974).
[11] A.R. Jule, *Chemistry of zeolites and catalysis*, (American Chemical Society,1976).
[12] C.B. Amphlett, *Inorganic ion exchangers*, (Elsevier Publishing Company, Amsterdam, London, New York, 1964).
[13] A.Yu. Lonin, V.V. Levenets, O.P. Omelnik, and A.O. Shchur, "Removal of a mixture of Cs, Sr and Co cations from an aqueous solution using composite sorbents based on natural and synthetic zeolites", JRNC, **331**, 5517 (2022). https://doi.org/10.1007/s10967-022-08637-y
[14] T.-J. Liang, and C.-N. Hsu, "Sorption of Cesium and Strontium on Natural Mordenite", Radiochimica Acta, **61**, 105 (1993). https://doi.org/10.1524/ract.1993.61.2.105
[15] K.M. Abd El-Rahman, M.R. El-Sourougy, N.M. Abdel-Monem, and I.M. Ismail, Journal of Nuclear and Radiochemical Sciences, **7**(2), 21 (2006). https://doi.org/10.14494/jnrs2000.7.2_21
[16] T. Abdollahi, J. Towfighi, and H. Rezaei-Vahidian, Environmental Technology & Innovation, **17**, 100592 (2020). https://doi.org/10.1016/j.eti.2019.100592
[17] Y. Izosimova, I. Gurova, I. Tolpeshta, M. Karpukhin, S. Zakusin, O. Zakusina, A. Samburskiy, and V. Krupskaya, "Adsorption of Cs(I) and Sr(II) on Bentonites with Different Compositions at Different pH", Minerals, **12**, 862 (2022). https://doi.org/10.3390/min12070862
[18] X.-H. Fang, F. Fang, C.-H. Lu, and L. Zheng, Nuclear Engineering and Technology, **49**(3), 556 (2017). https://doi.org/10.1016/j.net.2016.11.008
[19] A.Yu. Lonin, V.V. Levenets, O.P. Omelnik, A.O. Shchur, JRNC, **329**, 135 (2021), https://doi.org/10.1007/s10967-021-07762-4
[20] V.V. Levenets, A.Yu. Lonin, O.P. Omelnik, A.O. Shchur, JECE, **4**(4), 3961(2016), https://doi.org/10.1016/j.jece.2016.09.011
[21] A.Yu. Lonin, V.V. Levenets, I.M. Neklyudov, A.O. Shchur, JRNC, **303**, 831 (2015), https://doi.org/10.1007/s10967-014-3597-9
[22] V.V. Levenets, A.Yu. Lonin, O.P. Omelnik, and A.O. Shchur, X-Ray Spectrometry, **44**(6), 447 (2015), https://doi.org/10.1002/xrs.2626

ВПЛИВ КОНКУРУЮЧИХ ІОНІВ НА МУЛЬТИСОРБЦІЮ (Cs^+, Sr^{2+}) КОМПОЗИЦІЙНИМИ СОРБЕНТАМИ НА ОСНОВІ ПРИРОДНОГО ТА СИНТЕТИЧНИХ ЦЕОЛІТІВ

О.Ю. Лонін, В.В. Левенець, О.П. Омельник, А.О. Щур
Національний науковий центр «Харківський фізико-технічний інститут»
вул. Академічна, 1, 61108, Харків, Україна

У ході досліджень вивчався вплив конкуруючих іонів (Na+) на мультисорбцію (Cs+, Sr^{2+}) композиційними сорбентами на основі природних і синтетичних цеолітів у статичних умовах. Встановлено, що максимальна концентрація конкуруючих іонів (0,4 г NaCl на 100 мл розчину) призводить до зниження сорбції цезію на 20%, а сорбції стронцію – на 10%. При цьому зберігаються високі показники сорбції цезію та стронцію. Так, для композиційного сорбенту (кліноптилоліт – 30%: цеоліт NaX – 70%) сорбція цезію становила 67,9%, а сорбція стронцію – 87,6%. Аналітична методика була розроблена на основі методу PIXE (Індуковане протонами рентгенівське випромінювання) і дозволила якісно та кількісно визначати вміст ізотопів. Робота була виконана на аналітичному ядерно-фізичному комплексі «Сокіл». Енергетичний діапазон електростатичного прискорювача 200-2000 кеВ. Комплекс дозволяв проводити всі основні методи аналізу за допомогою іонних пучків. Мішені розміщувалися на виході, в камері для PIXE. Для проведення вимірювань в камері створювався вакуум з тиском 10^{-4} Па. Для збудження атомів цезію, стронцію використовувався пучок протонів з енергією Ep≈1400 кеВ. Характеристичне рентгенівське випромінювання L-серії атомів цезію та K-серії атомів стронцію реєструвалося двома детекторами: XR-100CR Si-PIN X-Ray та Ge(HP). Як кількісну характеристику взаємодії сорбентів з цезієм, стронцієм використовували коефіцієнт сорбції (Sorption, %).

Ключові слова: *цезій; стронцій; рідкі радіоактивні відходи; цеоліти; статична сорбція*

East European Journal of Physics. **1.** 130-134 (2023)
DOI:10.26565/2312-4334-2023-1-16 ISSN 2312-4334

MONITORING OF RADIATION DEFECTS RECOVERY IN $MgAl_2O_4$ DURING ANNEALING BY OPTICAL SPECTROSCOPY[†]

Yurii H. Kazarinov[a,b,*], Ivan G. Megela[c,§], Oksana M. Pop[c,‡]
[a]*V.N. Karazin Kharkiv National University, Kharkiv, Ukraine*
[b]*NSC "Kharkov Institute of Physics and Technology" of NASU, Kharkiv, Ukraine*
[c]*Institute of Electron Physics of NASU, Uzhgorod, Ukraine*
**Corresponding author e-mail: yu.kazarinov@karazin.ua*
[§]*E-mail: megela.i.g@gmail.com,* [‡]*E-mail: pop.ksenja@gmail.com*
Received January 4, 2023; revised January 25, 2023; accepted January 27, 2023

The extraordinary radiation resistance of single crystals and ceramics of magnesium-aluminum spinel to neutron irradiation is known, but the mechanisms that provide it are not yet fully understood. Irradiation of crystals with fast electrons creates defects partially similar to defects in neutron irradiation. The difference in the destructive effect is the significant level of ionization during electron irradiation. Therefore, to compare the results of irradiation by different sources, it is necessary to determine the parameters of radiation defects. One of them is the conditions of radiation damage recovery. When irradiating the crystals with electrons with an energy of 12.5 MeV to a fluence of $6.8 \cdot 10^{16}$ eV/cm^2, the concentration of defects such as F-centers $2.6 \cdot 10^{16}$ cm^{-3} and V-centers $3 \cdot 10^{17}$ cm^{-3} was obtained. TSL and optical absorption spectroscopy methods were used to determine the state of radiation defects in crystals during annealing. Since annealing at temperatures above 900 K leads to complete discoloration of all optically active centers, therefore, to determine the effect of annealing at higher temperatures, the crystals after annealing were irradiated with ultraviolet light. At temperatures above 900 K, cationic disorder begins to increase, but annealing at 1010 K for 30 minutes was not enough to completely restore the damage to the crystal lattice created by electron irradiation. This is expected, given the characteristic relaxation time of cation disorder, which reaches 1000 hours at this temperature. However, increasing the annealing temperature to 1050 K, in addition to the recovery of radiation defects, creates a noticeable additional difference in TSL, probably due to the formation of complexes from residual F-centers. However, determining the difference between irradiated and non-irradiated crystals gives a difference in the concentration of F-centers less than 10^{15} cm^{-3}.
Keywords: *Spinel; Electron Irradiation; Radiation Defects; Annealing; Thermoluminescence*
PACS: 61.80.Fe; 78.60.Kn; 61.72.jn

INTRODUCTION

Magnesium-aluminum spinel ($MgAl_2O_4$) is an extremely resistant to ion and neutron irradiation insulator with a wide bandgap. Crystals and ceramics can withstand neutron irradiation at moderate fluxes up to fluences of $2.49 \cdot 10^{23}$ n/cm^2 without appreciable change in sample size [1]. Although the optical and dielectric properties of spinel are very sensitive to ionizing irradiation [2] ceramics and spinel powders are considered for use [3] and are used [4] under conditions of powerful gamma, neutron and ion irradiation. Doses and levels of damage of 249 d.p.a., which were achieved at the FFTF reactor, are unattainable for other irradiation devices, except for ion irradiation, but it has its disadvantages related to the small depth of ion penetration. If the thin damaged layer can still be dealt with by experimental methods [5], there remains the implantation of ions that are not an element of the crystal and the temperature peaks when using heavy ions.

Irradiation by electrons compared to neutron irradiation is much more accessible. And because of the relatively small interaction cross-section of fast electrons, unlike ion irradiation, it makes it possible to obtain a practically uniform distribution of defects over the thickness of the samples. But the consequence is a relatively low rate of defect creation, which usually does not exceed one defect per electron. In addition, the beam current during irradiation is limited by the power of ionization losses of electrons in the crystal. The fact that the electrons predominantly (more than 99%) spend their energy on ionization and only a small fraction on defect creation is a feature to be taken into account when comparing experiments with different irradiation sources [6].

One of the characteristics of radiation defects is their destruction temperature. Since Schottky defects are the dominant type for spinel [7], the creation of Frenkel pairs during irradiation creates a complex set of pairs of defects of both types, some of which recombine during irradiation, preventing the creation of large complexes of defects and dislocations [8]. For neutron irradiated crystals, the temperature of the beginning of vacancy mobility and dislocation destruction is about 1000 K [9]. The trap depth for the vacancy mobility is determined as 2±0.7 eV.

Annealing of optically active centers in crystals allows the comparison of optical and ESR spectral data [10], but both techniques dealt with an electron bound to the defect rather than to the defect itself. In [11] annealing of spinel single crystals after electron irradiation at only 900 K resulted in complete bleaching of the radiation-induced absorption. In work [12] it is shown that after annealing to 750 K all optically active centers in the crystals after neutron irradiation are destroyed, but a significant concentration of defects remains. Therefore, elucidation of conditions and possibility of

[†] ***Cite as:*** Y.H. Kazarinov, I.G. Megela, and O.M. Pop, East Eur. J. Phys. **1**, 130 (2023), https://doi.org/10.26565/2312-4334-2023-1-16

restoration of damages of crystals after irradiation by relativistic electrons has both fundamental and applied importance concerning possibility of prolongation of use of crystals in radiation conditions and reuse of crystals in experiments on irradiation.

EXPERIMENTAL DETAILS

Electron irradiation was performed on an M-30 microtron at Institute of Electron Physics of NAS of Ukraine [13] with an electron energy of 12.5 MeV and a current density of 3 μA/cm^2 up to a fluence of $6.8 \cdot 10^{16}$ e/cm^2. The sample was glued with thermal grease KTP-19 on an aluminum plate with a thickness of 2 mm and located at a distance of 5 cm from the exit window of the accelerator. With addition of intense air blowing, this ensured that the temperature of the sample during irradiation did not exceed 20°C.

Measurements of the curves of thermostimulated luminescence (TSL) induced by heating samples at a rate of 0.5 K/s up to 575 K were performed after the half hour delay to partial decay of phosphorescence. The integral thermoluminescence yields were performed using a FEU-106 photoelectron multiplier (spectral response 180-800 nm) operating in the photon count mode.

Before TSL measurements (except for electron irradiated sample) samples were irradiated with UV lamp DDS-30 (analogue of L2(D)2) for filling electron and hole traps. Distance between lamp and samples was 50 mm.

High-temperature annealing was carried out in a tubular quartz furnace insulated from the ends with fireclay. The temperature of the samples was controlled by a chromel-alumel thermocouple located in the sample holder. Cooling from the maximum temperature to 200°C took place in the furnace for an hour, and then in the open air.

Optical absorption was measured in the range 1.2–6.4 eV using a single beam spectrophotometer SF-46 with manual correction of residual phosphorescence.

RESULTS AND DISCUSSION

The optical absorption spectra of single crystals before and after irradiation with electrons with energy of 12.5 MeV and fluence of $6.8 \cdot 10^{16}$ cm^{-2} are shown in Fig. 1. As can be seen, the spectrum shows two well-known absorption bands at 3 eV - hole centers on cation vacancies and 5.3 eV - F-centers. The integrated glow curve of this sample is also quite typical for nominally pure spinel single crystals of stoichiometric composition (Fig.2). It contains one high-intensity broad maximum at 500 K which is very similar to the TSL curve after gamma irradiation [14,15]. In neutron-irradiated crystals, the spinel light curve has weak peaks at 440, 490 K and a prominent peak at 630 K [16]. This difference could be caused by the high level of ionization during electron and gamma irradiation.

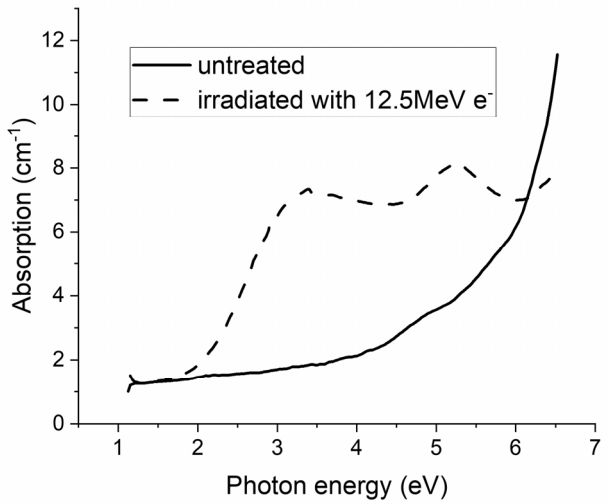

Figure. 1. Optical absorption spectra of $MgAl_2O_4$ single crystal before and after irradiation with 12.5 MeV electrons to fluence $6.8 \cdot 10^{16}$ e/cm^2

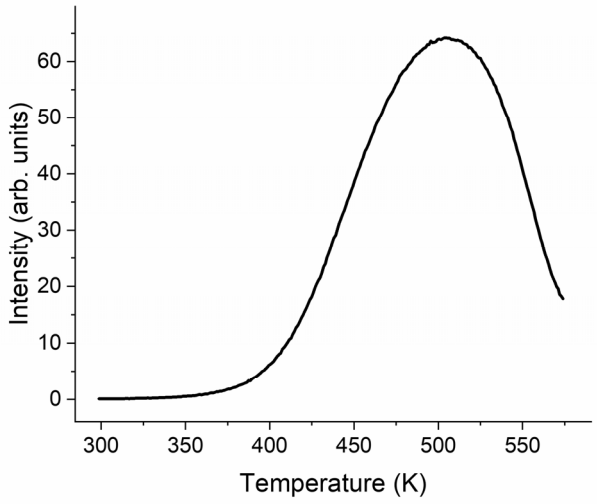

Figure. 2. TSL glow curve of $MgAl_2O_4$ single crystal irradiated with 12.5 MeV electrons to fluence $6.8 \cdot 10^{16}$ e/cm^2

As a result of annealing to 575 K, the absorption spectrum of the crystal partially discolored. The spectra of radiation stimulated absorption after irradiation and annealing are shown in Fig. 3. Also, thin lines show the decomposition of the spectra into separate bands according to [17]. As can be seen, partial annealing caused 50% loss of absorption of V-centers, and almost complete decolorization of F^+ and F-centers. Since an annealing at a temperature of at least 970 K is required to fully restore the absorption spectrum, the sample irradiated by electrons was annealed at 1010 K for 30 min.

To analyze the results of such annealing, the crystal after slow cooling was irradiated with UV light for 30 min. and after an additional 30 min. the thermoluminescence was measured (see Fig. 4). For comparison, the thermal luminescence curve of the crystal without electron irradiation and annealing is also shown. It can be seen that the first peak at 410 K is almost the same, but at higher temperature (peak at 650-700 K) the crystal irradiated by electrons has much more intense

luminescence. In order to return the crystal to the initial state, an additional annealing was carried out at a temperature of 1050 K. This significantly reduced the intensity of the high-temperature maximum and it became even smaller than the corresponding maximum in the initial crystal. But it caused a shift of the first maximum towards higher temperatures.
To further verify the effect of irradiation and annealing on the crystal state, both samples were irradiated with UV light after annealing at 1050 K. Fig. 5 shows the absorbance for both samples, where it can be seen that the absorbance (concentration of optically active centers) due to hole centers on cation vacancies and anti-structure defects is identical. There is a very weak difference in the absorption of electron-type optically active centers: antisite defects and anion vacancies.

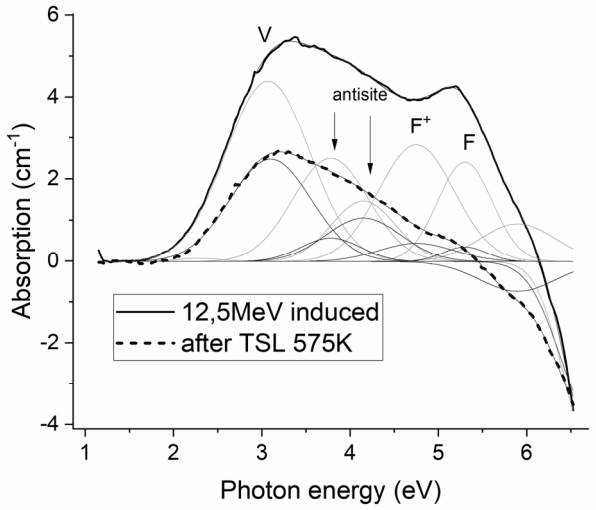

Figure. 3. Optical absorption spectra of $MgAl_2O_4$ single crystal irradiated with 12.5 MeV electrons to fluence $6.8 \cdot 10^{16}$ e/cm^2 and after annealing to 575 K during TSL measurement

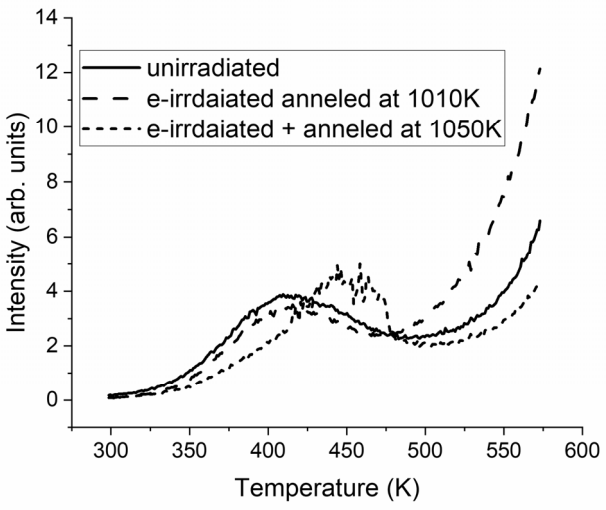

Figure. 4. TSL glow curve of UV irradiated $MgAl_2O_4$ single crystals: unirradiated and irradiated with 12.5 MeV electrons to fluence $6.8 \cdot 10^{16}$ e/cm^2 and annealed to different temperatures during 30 min

It is shown in more detail in Fig. 6 in the form of difference of absorption spectra of two crystals (with and without irradiation) in the same state. It can be seen that the effect of electron irradiation after annealing to 1050 K on the formation of optically active centers is very weak both for the annealed state and after UV irradiation.

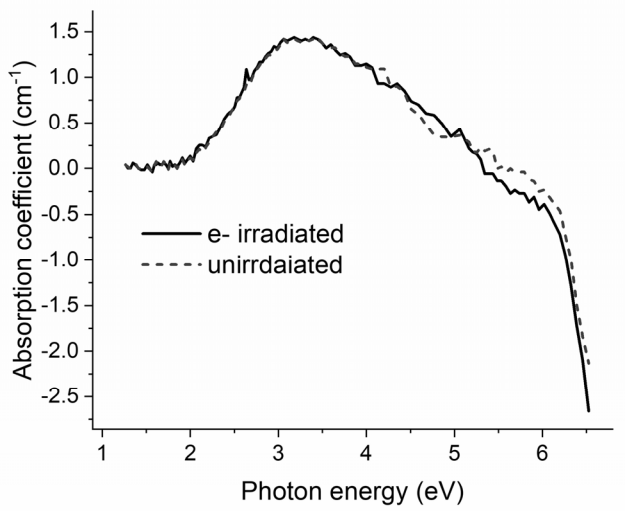

Figure 5. UV induced optical absorption spectra of $MgAl_2O_4$ single crystal with and without irradiation with 12.5 MeV electrons to fluence $6.8 \cdot 10^{16}$ e/cm^2 and annealing at 1050 K for 30 min

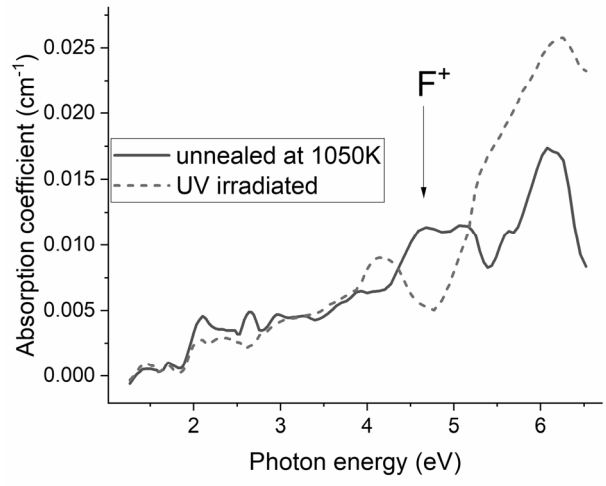

Figure 6. Difference optical spectra of irradiated and unirradiated $MgAl_2O_4$ crystals after annealing to 1050 K and subsequent UV irradiation

The difference between irradiated and non-irradiated crystals is small, slightly exceeding the measurement error of the spectrophotometer. Only one very weak band corresponding to F^+-centers can be approximately identified in the spectra, but their concentration determined by the Smakula formula [18] does not exceed $1.5 \cdot 10^{14}$ cm^{-3}. Absence of differences in induced absorption spectra in the region of maxima corresponding to antisite defects indicates that although

the annealing temperature exceeded the threshold of cation mobility and increasing of inversion the changes in TSL glow curve (Fig. 4) are rather related to the formation of complexes from residual defects.

CONCLUSIONS

Sequential annealing of defects in $MgAl_2O_4$ single crystals after 12.5 MeV electron irradiation was carried out. It was found that 30 min. of annealing at 1010 K was not sufficient for the complete recovery of radiation defects. Additional annealing at 1050 K of $MgAl_2O_4$ single crystals irradiated with intermediate fluence electrons practically restores the crystal state to the initial level.

It is also shown that annealing at 1050 K for 30 min., besides the restoration of defects, introduces noticeable changes in the crystal, which may be associated with an increase in inversion. However, the residual difference in F-centers concentration at $1.5 \cdot 10^{14}$ cm^{-3} rather indicates the formation of complexes from residual defects. Therefore, the optimization of the annealing process with respect to temperature, duration and cooling regime requires further investigation.

Funding. This work was supported by the Ministry of Education and Science of Ukraine (Joint Ukrainian – Latvian Project 0122U200281).

ORCID IDs

Yurii H. Kazarinov, https://orcid.org/0000-0001-5143-8545; **Ivan G. Megela**, https://orcid.org/0000-0003-3388-3535
Oksana M. Pop, https://orcid.org/0000-0002-5690-1030

REFERENCES

[1] F.A. Garner, G.W. Hollenberg, F.D. Hobbs, J.L. Ryan, Z. Li, C.A. Black, and R.C. Bradt, "Dimensional stability, optical and elastic properties of $MgAl_2O_4$ spinel irradiated in FFTF to very high exposures", J. Nucl. Mater. **212–215**, 1087–1090 (1994). https://doi.org/10.1016/0022-3115(94)91000-6

[2] J.-M. Costantini, G. Lelong, M. Guillaumet, S. Takaki, and K. Yasuda, "Color-center formation and thermal recovery in X-ray and electron-irradiated magnesium aluminate spinel", J. Appl. Phys. **124**, 245901 (2018). https://doi.org/10.1063/1.5055230

[3] E.F. Daly, K. Ioki, A. Loarte, A. Martin, A. Brooks, P. Heitzenroeder, M. Kalish, C. Neumeyer, P. Titus, Y. Zhai, Y. Wu, H. Jin, F. Long, Y. Song, Z. Wang, R. Pillsbury, J. Feng, T. Bohm, M. Sawan, and J. Preble, "Update on design of the ITER in-vessel coils", Fusion Sci. Technol. **64**, 168–175 (2013). https://doi.org/10.13182/FST13-A18073

[4] J. Delauter, J.C. Dekamp, A.F. Zeller, C.Y. Gung, and J.V. Minervini, "Magnetic testing of a superferric dipole that uses metal-oxide insulated CICC", IEEE Trans. Appl. Supercond. **19**, 1092–1094 (2009). https://doi.org/10.1109/TASC.2009.2019217

[5] D. Simeone, C. Dodane-Thiriet, D. Gosset, P. Daniel, and M. Beauvy, "Order-disorder phase transition induced by swift ions in $MgAl_2O_4$ and $ZnAl_2O_4$ spinels", J. Nucl. Mater. **300**, 151–160 (2002). https://doi.org/10.1016/S0022-3115(01)00749-8

[6] T. Shikama, and G.P. Pells, "A comparison of the effects of neutron and other irradiation sources on the dynamic property changes of ceramic insulators", J. Nucl. Mater. **212–215**, 80–89 (1994). https://doi.org/10.1016/0022-3115(94)90036-1

[7] S.S. De Souza, F. Ayres, and A.R. Blak, "Simulation models of defects in Mg Al_2O_4:Fe^{2+}, Fe^{3+} spinels", Radiat. Eff. Defects Solids. **156**, 311–316 (2001). https://doi.org/10.1080/10420150108216911

[8] C. Kinoshita, K. Fukumoto, K. Fukuda, F.A. Garner, and G.W. Hollenberg, "Why is magnesia spinel a radiation-resistant material?", J. Nucl. Mater. **219**, 143–151 (1995). https://doi.org/10.1016/0022-3115(94)00388-2

[9] K. Yasuda, C. Kinoshita, K. Fukuda, and F.A. Garner, "Thermal stability and kinetics of defects in magnesium aluminate spinel irradiated with fast neutrons", J. Nucl. Mater. **283–287**, 937–941 (2000). https://doi.org/10.1016/S0022-3115(00)00118-5

[10] A. Lushchik, E. Feldbach, E.A. Kotomin, I. Kudryavtseva, V.N. Kuzovkov, A.I. Popov, V. Seeman, and E. Shablonin, "Distinctive features of diffusion-controlled radiation defect recombination in stoichiometric magnesium aluminate spinel single crystals and transparent polycrystalline ceramics", Sci. Rep. **10**, 1–9 (2020). https://doi.org/10.1038/s41598-020-64778-8

[11] A. Lushchik, S. Dolgov, E. Feldbach, R. Pareja, A.I. Popov, E. Shablonin, and V. Seeman, "Creation and thermal annealing of structural defects in neutron-irradiated $MgAl_2O_4$ single crystals", Nucl. Instruments Methods Phys. Res. Sect. B Beam Interact. with Mater. Atoms, **435**, 31–37 (2018). https://doi.org/10.1016/j.nimb.2017.10.018

[12] V.T. Gritsyna, and Y.G. Kazarinov, "Thermal stability of radiation-induced optical centers in non-stoichiometric spinel crystals", Nucl. Instruments Methods Phys. Res. Sect. B Beam Interact. with Mater. Atoms, **250**, 349–353 (2006). https://doi.org/10.1016/j.nimb.2006.04.136

[13] M.I. Romanyuk, J.J. Hainysh, Y. Plakosh, V. Kovtun, O.M. Turhovsky, G.F. Pitchenko, I.G. Megela, M.V. Goshovsky, O.O. Parlag, V.T. Maslyuk, and N.I. Svatiuk, "Microtron M-30 For Radiation Experiments: Formation And Control Of Irradiation Fields", PAST, **3**, 137–143 (2022). https://doi.org/10.46813/2022-139-137

[14] A. Lorincz, M. Puma, F.J. James, and J.H. Crawford, "Thermally stimulated processes involving defects in γ- and x-irradiated spinel ($MgAl_2O_4$)", J. Appl. Phys. **53**, 927–932 (1982). https://doi.org/10.1063/1.330562

[15] Y. Kazarinov, V. Kvatchadze, V. Gritsyna, M. Abramishvili, Z. Akhvlediani, M. Galustashvili, G. Dekanozishvili, T. Kalabegishvili, and V. Tavkhelidze, "Spectroscopic studies of defects in gamma- and neutron-irradiated magnesium aluminates spinel ceramics", PAST, **5**, 8–13 (2017). https://vant.kipt.kharkov.ua/ARTICLE/VANT_2017_5/article_2017_5_8.pdf

[16] V.T. Gritsyna, I. V. Afanasyev-Charkin, V.A. Kobyakov, and K.E. Sickafus, "Neutron irradiation effects in magnesium-aluminate spinel doped with transition metals", J. Nucl. Mater. **283–287**, 927–931 (2000). https://doi.org/10.1016/S0022-3115(00)00196-3

[17] V.T. Gritsyna, I. V. Afanasyev-Charkin, Y.G. Kazarinov, and K.E. Sickafus, "Optical transitions in magnesium aluminate spinel crystals of different compositions exposed to irradiation", Nucl. Instruments Methods Phys. Res. Sect. B Beam Interact. with Mater. Atoms. **218**, 264–270 (2004). https://doi.org/10.1016/j.nimb.2004.02.002

[18] D.L. Dexter, "Absorption of light by atoms in solids", Phys. Rev. **101**, 48–55 (1956). https://doi.org/10.1103/PhysRev.101.48

МОНІТОРИНГ ВІДНОВЛЕННЯ РАДІАЦІЙНИХ ДЕФЕКТІВ В $MgAl_2O_4$ ПРИ ВІДПАЛІ МЕТОДОМ ОПТИЧНОЇ СПЕКТРОСКОПІЇ

Юрій Г. Казарінов[a,b], Іван Г. Мегела[c], Оксана М. Поп[c]

[a]*Харківський національний університет імені В.Н. Каразіна, Харків, Україна*

[b]*ННЦ "Харківський фізико-технічний інститут" НАН України, Харків, Україна*

[c]*Інститут електронної фізики НАН України, Ужгород, Україна*

Відома надзвичайна радіаційна стійкість монокристалів і кераміки магнієво-алюмінієвої шпінелі до нейтронного опромінення, але механізми, які її забезпечують, ще остаточно не з'ясовані. Опромінення кристалів швидкими електронами створює дефекти, частково подібні до дефектів при нейтронному опроміненні. Відмінність у руйнівній дії полягає в значному рівні іонізації при електронному опроміненні. Тому, для порівняння результатів опромінення різними джерелами необхідно визначати параметри радіаційних дефектів. Одним з них є температурні умови відновлення радіаційних пошкоджень. При опроміненні кристалів електронами з енергією 12,5 МеВ до флюенсу $6{,}8\cdot10^{16}$ е/см^2 отримано концентрацію дефектів типу F-центрів $2{,}6\cdot10^{16}$ см$^{-3}$ та V-центрів $3\cdot10^{17}$ см$^{-3}$. Для визначення стану радіаційних дефектів у кристалах під час відпалу використовувались методи ТСЛ та оптичної абсорбційної спектроскопії. Оскільки відпал при температурах вище 900 К призводить до повного знебарвлення всіх оптично активних центрів, тому для визначення впливу відпалу при більш високих температурах кристали після відпалу опромінювали ультрафіолетовим світлом. При температурах вище 900 К починає зростати катіонне невпорядкування, але відпалу при 1010 К протягом 30 хвилин виявилося недостатньо для повного відновлення пошкоджень кристалічної гратки, створених електронним опроміненням. Це очікувано, враховуючи характерний час релаксації катіонного невпорядкування, який при цій температурі сягає 1000 годин. Однак підвищення температури відпалу до 1050 К, окрім відновлення радіаційних дефектів, створює помітну додаткову різницю в ТСЛ, ймовірно, за рахунок утворення комплексів із залишкових F-центрів. Однак визначення різниці між опроміненими і неопроміненими кристалами методом оптичної спектрофотометрії дає різницю в концентрації F-центрів менше за 10^{15} см$^{-3}$.

Ключові слова: *шпінель; електронне опромінення; радіаційні дефекти; відпал; термолюмінесценція*

East European Journal of Physics. **1.** 135-145 (2023)
DOI:10.26565/2312-4334-2023-1-17 ISSN 2312-4334

INSINUATION OF ARRHENIUS ENERGY AND SOLAR RADIATION ON ELECTRICAL CONDUCTING WILLIAMSON NANO FLUIDS FLOW WITH SWIMMING MICROORGANISM: COMPLETION OF BUONGIORNO'S MODEL[†]

Muhammad Jawad
Department of Mathematics, The University of Faisalabad, Faisalabad 38000, Pakistan
E-mail: muhammad.jawad@tuf.edu.pk
Received October 18, 2022; revised December 13, 2022; accepted December 23, 2022

The enriched thermal mechanisms and progressive of nanomaterial has enthused scientists to give devotion to this area in current days. The versatile and synthesizing utilization of such particles embrace energy production, solar systems, heating and cooling monitoring processes, renewable energy systems, cancer treatments, hybrid-powered motors and Nano electronics. Furthermore, in this era of biotechnology and bioengineering, the bio convection of Nano fluids provides for some enthralling applications, such as enzymes, biosensors and biofuels. With such magnetic applications and attentions. A mathematical model is presented for evaluating the electrical conducting Williamson nano fluid with heat and mass transfer over a porous stretched sheet in the existence of bioconvection. The bioconvection of swimming microorganisms, thermal radiation, thermal conductivity and Arrhenius energy are new facets of this investigation. The higher order non-linear governing partial differential equations (PDEs) are solved by applying appropriate similarity variables and resulting couple of ordinary differential equations (ODEs) is produced. The developing set of ODEs is solved numerically by utilizing well known shooting technique with ND solve command in Wolfram MATHEMATICA and compare the result with pvb4c code in MATLAB. The graphs for different physical quantities of interest together with non-dimension velocity, temperature, concentration and density of micro-organisms profiles are discovered for involving parameters like magnetic parameter, Brownian motion, Rayleigh number, Peclet number, Bioconvective Lewis number, parameter of thermophoresis and buoyancy ratio parameter. The influence of numerous parameters on flow and heat transfer characteristics are debated.
Keywords: *Activation energy; Williamson Nano fluids; Chemical reaction; Thermal Radiation; Shooting method; Extending sheet; Thermal conductivity*
PACS: 47.10.-g, 47.10.A-, 47.10.ad

INTRODUCTION

Due to its enormous applications, the mass and heat transfer of boundary layer flow of non-Newtonian fluids through permeable medium due to a extending plate is of significant interest to researchers, engineers and scientists. Some good illustrations of its utilizations are the cooling of nuclear reactors, pipe industry, thinning of copper wire, annealing, solar collection, extraction of metals and extrusion process. The quick and convoluted process in tiny devices and gigantic machinery have generated a large problem of thermal discrepancy. Various additional approaches, like as fans and fins are utilized, but their utility is limited due to the enormous size. Maripala and Kishan [1] considered the effect of chemical diffusion and solar radiation on magneto un-steady flow and heat transport of nanofluid through a porous shrinking plate. Their outcome shows that the energy distribution diminishes with boosted in the suction parameter while nano concentration distribution rise. Over stretched surfaces, the effect of mixed convective mass and heat transport of MHD nanoparticles inserted in permeable sheet. Thermal boundary layer and energy profile diminish when the Prandtl number and dimensionless mass free convection parameter grow, according to their findings investigated by [2-8]. In 1995, Choi [9] proposed that nano-sized particles dispersed in a base fluid, dubbed nanofluid, have a higher heat transfer capacity than fluids lacking nano-sized particles. The present and prospective utilization of nano-sized particles in fluids is discussed by [10]. A single model cannot account for non-Newtonian fluid features. Also, the fundamental Naiver-Stokes equations cannot explain the rheological features of non-Newtonian fluids. A ample models have been established to address this issue. The rheological models that were proposed like Carreau, Ellis, power law, Cross and Williamson fluid model, etc. The Williamson fluid model is an example of a non-Newtonian fluid (liquid/gas) model with shear retreating behaviour, and it was predicted by Williamson [11]. Investigations [12–16] might be mentioned as current inquiries into the flow of magneto Williamson fluid.

The minimal quantity of strength required by chemical reactants to tolerate a significance chemical diffusion is known as activation energy. Bestman [17] investigated the inspiration of heat transfer and energy activation on Natural convection boundary layer through porous plate. Hamid et al. [18] explore the effect of chemical diffusion on time depended flow of electrical conducting Williamson nanofluid in the occurrence of Arrhenius energy. Anuradha and Sasikala [19] examined the effect of energy activation and binary chemical reaction on magneto flow of nanofluid through porous shrinking plate with convective flow. Dhlamini et al. [20] established the mathematical model for mixed convective nanofluid flow in the existence of chemical diffusion and energy with convective boundary conditions. Awad et al. [21] scrutinized the insinuation of Arrhenius energy and binary chemical diffusion on rotating flow of time in depended nanofluid in the occurrence of energy activation. Mustafa [22] and Huang [23] also looked into the effect of

[†] ***Cite as:*** M. Jawad, East Eur. J. Phys. **1**, 135 (2023), https://doi.org/10.26565/2312-4334-2023-1-17

Arrhenius energy on electrical conducting flow of nanoparticle passing through a both permeable horizontal and vertical cylinder. Many researchers like [24–27] describes additional research on the influence of energy activation on MHD flow of non-Newtonian fluids under various geometries. Their figures show that the concentration of nanoparticles rises with rise in activation energy as well.

The sensation of alive microorganisms deeper than water swimming upward in suspensions is known as bioconvection. Bioconvection have significance utilization in biotechnology and biological systems such as enzyme biosensors, purify cultures and living cells [28]. Through a horizontal tube, Raees et al. [29] investigated an time depended flow of magnetized bioconvective nanofluid containing swimming gyrotactic microorganisms. The bioconvective flow of MHD magnetized nano fluid with mass and heat transfer with swimming microorganisms across a rounded vertical cone was quantitatively discovered by Siddiqa et al. [30]. Abbasi et al. [31] described in detail the bioconvection stream of viscoelastic nanoparticles caused by motile microorganisms passing through a turning extending disc with convective boundary condition and zero mass flux as well as prominent parameters' inspirations on Nusselt number, temperature, local density, velocity and Sherwood number. Chu et al. [32] analyzed the impact of stream of bioconvection on electrical conducted fluid over extending plate with chemical reaction, Brownian motion, thermophoresis diffusion, activation energy and significance of motile microorganisms are taken into account. The consequences of a nonlinear thermal radiation and magnetic field on bioconvective magnetized nanofluid flow via the upper surface of a paraboloid of revolution were studied by Makinde et al. [33]. Henda et al. [34] looked considered the magnetic bioconvection flow of time depended fluid past through nonlinear expanding cylinder with a heat source, nonlinear thermal radiation and Arrhenius energy. This investigation illustrates the electrical conducting flow of Williamson nanofluid flow having the insertion of swimming microorganisms through a stretchy sheet. The influence of energy activation, chemical reaction parameter, Buoyant force, and thermal conduction is also a part of this study. The effect of gravitational body forces is also taken under attention in this analysis. The shooting method has been applied to compute the numerical outcomes. Furthermore, a graphical illustration of numerous prominent parameters are also presented in this research.

PROBLEM STATEMENT

Steady two-dimensional inviscid flow of magneto Williamson nanofluid with thermal radiation and Arrhenius energy embedded in a permeable stretchable plate is considered in the occurrence of swimming microorganism and thermal conductivity. The fluids flow owing to a extending sheet with non-zero mass flux. Because of the stretched sheet, it is expected that the flow will behave linearly. Here u and v are the part of velocity along x and y directions. Our mathematical problem characterizes the fundamental equations of mass conservation, equation of flow, temperature equation, nanofluid concentration equation and motile density equation in Cartesian coordinates. The mathematical highly nonlinear governing equations for the stated problems are given below [35-36]:

The equation of mass conservation

$$u_x + v_y = 0. \tag{1}$$

The Equation of momentum

$$uu_x + vu_y = \nu u_{yy} + \frac{1}{\rho_f}\left[\begin{array}{l}(1-C_\infty)(T-T_\infty)\beta\rho_f - \\ (\rho_p - \rho_f)(C-C_\infty) - \\ \gamma(n-n_\infty)(\rho_m - \rho_r)\end{array}\right] g - \frac{\sigma_e B_0^2 u}{\rho_f} + \Gamma u_y u_{yy} - \frac{\nu u}{K}. \tag{2}$$

Subjected to

$$v = 0,\ u = ax\ ,\ u \to U = ax$$

The Equation Temperature

$$uT_x + vT_Y = \frac{k}{(\rho c)_f}\left(T_{yy}\right) + \frac{(\rho c)_p}{(\rho c)_f}\left\{\frac{D_T}{T_\infty}\left(T_y\right)^2 + D_B C_y T_y\right\} - \frac{1}{(\rho c)_f} q_{r_y} + \frac{Q_0}{(\rho c)_f}\left(T - T_\infty\right). \tag{3}$$

Subjected to

$$T = T_W \ \ as \ \ y \to 0\ ,$$

$$T \to T_\infty \ \ as \ y \to \infty.$$

The Equation Concentration

$$uC_x + vC_y = D_B C_{yy} + \frac{D_T}{T_\infty} T_{yy} - K_0\left(C - C_\infty\right)\left(\frac{T}{T_\infty}\right)^n \exp\left(-\frac{E_a}{kT}\right). \tag{4}$$

Subjected to

$$C = C_W \ \ as \ \ y \to 0\ .$$

$$C \to C_\infty \ \ as \ \ y \to \infty .$$

The Equation of Density of microorganism

$$un_x + vn_y + \frac{bW_c}{C_W - C_\infty}\left[n_y C_{yy} \right] = D_m n_{yy} . \tag{5}$$

Subjected to

$$n = n_W \ \ as \ \ y \to 0 ,$$
$$n \to n_\infty \ \ as \ \ y \to \infty .$$

In these governing equations the component of velocity u and v are assumed in x and y direction respectively, ρ_f is the density of base fluid, ν is the viscosity, σ^* is the electrical intensity, k^* is the absorption constant, β the volume expansion coefficient, g is gravity, ρ_p density of microorganisms particles, $\dot{\gamma}$ represents the volume of the microorganism, n is the concentration of the microorganism in the fluid T is temperature of nanofluid, α is thermal diffusivity, $(\rho c)_f$ heat capacity of liquid, $(\rho c)_p$ effective heat capacity of nanoparticles, q_r is radiative heat flux, W_c is the maximum cell swimming speed, D_B for Brownian diffusivity, D_T for thermophoretic diffusion coefficient, k_c chemical reaction parameter and D_m is the diffusivity of microorganisms.

where $k_c\left(C - C_\infty\right)\left(\frac{T}{T_\infty}\right)^n \exp\left(-\frac{E_a}{kT}\right)$ represents the Arrhenius expression. The temperature dependent thermal conductivity is expressed as

$$k = k_\infty \left(1 + \varepsilon \frac{T - T_\infty}{T_{w-} T_\infty}\right), \tag{6}$$

According to radiative heat flux theory

$$q_r = \frac{-4\sigma^*}{3k^*}\frac{\partial T^4}{\partial y}, \tag{7}$$

where k^* stands for absorption coefficient and σ^* denotes Stefan Boltzman Constant. Using expansion of Talyer's series about T_∞ we get

$$T^4 = 4T_\infty^{\ 3} T - 3T_\infty^{\ 4} . \tag{8}$$

The utilization of Eqs. (11-12) in (4), we have

$$uT_x + vT_Y = \frac{k}{(\rho c)_f}\left(T_{yy}\right) + \frac{(\rho c)_p}{(\rho c)_f}\left\{\frac{D_T}{T_\infty}\left(T_y\right)^2 + D_B C_y T_y\right\} + \frac{16\sigma^* T_\infty^3}{3k^*(\rho c)_f}\frac{\partial^2 T}{\partial y^2} + \frac{Q_0}{(\rho c)_f}\left(T - T_\infty\right). \tag{9}$$

Let us implement the following similarity approaches, to transform partial differential equations (PDEs) to Ordinary differential equations (ODEs) [30-31]:

$$\psi = (a\nu)^{\frac{1}{2}} x f(\eta),\ \eta = \left(\frac{a}{\nu}\right)^{\frac{1}{2}} y,\ \text{and}\ C = C_\infty + \left(C_w - C_\infty\right)\phi(\eta),\ \ T = T_\infty + \left(T_w - T_\infty\right)\theta(\eta),\ \ n = n_\infty + \left(n_w - n_\infty\right)\chi(\eta),$$

where $\psi(x, y)$ is the stream line function defined as $u = \psi_y$ and $v = -\psi_x$, which tropically fulfills the equation of mass conservation and η is the similarity variable. Equations (02) – (05) reduce to

$$f''' + ff'' - f'^2 + Wef'''[\eta] f''[\eta] - (M + K_1) f' + \lambda\left(\theta - N_r\phi - N_c\chi\right) = 0, \tag{10}$$

$$\left(1 + \frac{4Rd}{3}\right)\theta''[\eta] + p_r f[\eta]\theta'[\eta] + p_r Nt\theta'^2[\eta] + p_r Nb\theta'[\eta]\phi'[\eta] + p_r \Delta\theta[\eta] = 0, \tag{11}$$

$$\phi''[\eta] + \Pr Lef[\eta]\phi'[\eta] + \left(\frac{N_t}{N_b}\right)\theta''[\eta] - \Pr Le\gamma\left(1 + \delta\theta[\eta]\right)^n \exp\left(\frac{-E}{1 + \delta\theta}\right)\phi[\eta] = 0, \tag{12}$$

$$\chi''[\eta]-P_e\chi[\eta]\phi'[\eta]-P_e\sigma\phi''[\eta]+P_e\chi'[\eta]\phi''[\eta]+S_cf[\eta]\chi'[\eta]=0 \tag{13}$$

Boundary condition becomes:

$$f(\eta)=S, f'(\eta)=\lambda, \chi(\eta)=1, \theta(\eta)=1, \phi(\eta)=1 \ as \ \eta\to 0 \tag{14}$$

$$f'(\eta)=1, \theta(\eta)=0, \phi(\eta)=0, \chi(\eta)=0 \ as \ \eta\to\infty \tag{15}$$

where $\gamma=\frac{K_0}{a}$ is chemical reaction parameter, $Le=\frac{\nu}{D_B}$ Lewis number, $\delta=\frac{T_w-T_\infty}{T_\infty}$ is temperature difference, $\lambda'=\frac{\beta\dot{\gamma}(1-C_\infty)(T_w-T_\infty)x^3}{aU_w}$ mixed convection parameter, $E=\frac{E_a}{kT_\infty}$ is activation energy, $Rd=\frac{4\sigma^*T_\infty^3}{k^*k_\infty}$ is thermal Radiation, $Nr=\frac{(\rho_p-\rho_f)(C_w-C_\infty)}{\beta\rho_f(1-C_\infty)T_\infty\beta}$ is buoyancy ratio parameter, $K_1=\frac{\nu}{aK}$ is porosity parameter, $P_r=\frac{\nu_f}{\alpha}$ is Prandtl number, $Nc=\frac{\dot{\gamma}(\rho_m-\rho_f)(n_w-n_\infty)}{\beta\rho_f(1-C_\infty)T_\infty}$ Rayleigh number, $\sigma=\frac{N_\infty}{N_w-N_\infty}$ is microorganism concentration difference, $Nb=\frac{D_B\tau(C_w-C_\infty)}{\nu}$ is Brownian motion, $\Delta=\frac{Q_0}{a(\rho_C)_f}$ is heat generation/absorption coefficients, $Nt=\frac{D_T\tau(T_w-T_\infty)}{T_\infty\nu}$ is thermophoresis parameters, $Pe=\frac{bW_c}{D_m}$ is Peclet number and $Sc=\frac{\nu}{D_n}$ is Schmidt number.

The physical quantities of interest are defined as

$$C_f=\frac{\tau_w}{\rho U_w^2}, Nu_x=\frac{xq_w}{k(T_w-T_\infty)}, Sh_x=\frac{xq_m}{D_B(C_w-C_\infty)}, Nn_x=\frac{xq_m}{D_n(N_w-N_\infty)} \tag{16}$$

$$C_f\,\mathrm{Re}_x^{1/2}=-f''(0), Nu_x\,\mathrm{Re}_x^{1/2}=-\theta'(0), Sh_x\,\mathrm{Re}_x^{1/2}=-\phi'(0), Nn_x\,\mathrm{Re}_x^{1/2}=-\chi'(0), \tag{17}$$

where $\mathrm{Re}_x^{1/2}=U_w\,x/\upsilon$ is the local Reynolds number.

NUMERICAL TECHNIQUE

In a daily life many mathematical models of equations are highly nonlinear differential equation. We knew that exact solution of extremely nonlinear differential equations is not usually possible. In case of boundary value problem, the shooting method is one of best and well know scheme among all other methods. Another characteristic of current method is to find boundary conditions by utilizing initial approximations. This procedure is straightforward sensitive and free from error or complexity.

CODE OF VALIDATION

Table 1 provides a critical study of the current findings of $-\theta'(0)$ and $-\varphi'(0$ for the different value of Nb (Brownian motion parameter) utilizing the bvp4c package in MATLAB. The critical study of these numerical findings in Table 1 reveals that the scheme is valid, M = 0.5, λ = 0.1, γ = 0, Nc = σ = 0.3, Sc = Pe = Le = 0.2 and Pr = 7. The assessment of outcomes in Table 1 shows the astonishingly considerable compositions of the current inquiry with the bvp4c (MATLAB) results, which motivates the investigator to tackle this problem with changes of nonlinear thermal radiation and chemical diffusion effects using a well-known shooting approach.

Table. 1. Comparison of $-\theta'(0)$ and $-\varphi'(0)$ with different value of Nb.

Parameter	bvp4c	Present [ND solve]	bvp4c	Present [ND solve]
Nb	$-\theta'(0)$		$-\varphi'(0)$	
0.1	1.15531	1.15531	0.71015	0.71015
0.2	0.82268	0.82268	0.42569	0.42569
0.3	0.56502	0.56502	0.22570	0.22570
0.4	0.37419	0.37419	0.09421	0.09421
0.5	0.23917	0.23917	0.01730	0.01730

RESULTS AND DISCUSSIONS

Where this section is equipped to explore the act of non-dimensional velocity profile $f'(\eta)$, energy profile $\theta(\eta)$, nanofluid concentration profile $\phi(\eta)$ and density $\chi(\eta)$ under the influence of several prominent parameters like chemical diffusion parameter γ, temperature difference δ, mixed convection parameter λ', energy activation E, thermal Radiation Rd, buoyancy ratio parameter Nr, porosity parameter K_1, Prandtl number P_r, Nc Rayleigh number, microorganism concentration difference σ, Brownian motion Nb, heat generation/absorption coefficients Δ, thermophoresis parameters Nt, bioconvection Lewis number Le, Harman number M and Peclet number Pe. Fig. 1 is demonstrated to assess the influence of Hartman number M on the velocity function $f'(\eta)$. Figure 1 depicts that the supplementing values of M causes retardation in the velocity profile Lorentz forces that are resistive forces are included in Hartman number. As M boost up, the Lorentz force enhanced causing in resistance of the flow of liquid as a result of velocities decline. The effect of Williamson parameter We against velocity distribution is plotted in Fig. 2 the increment in We decreases the fluid speed $f'(\eta)$, it is due to occurrence of buoyancy forces. An inverse relation between stretching λ and velocity field $f'(\eta)$ is obtained by Fig. 3, an increment in values of λ decreases the curve of $f'(\eta)$. Inspiration of Mixed convection Parameter on velocity distribution is plotted in Figure (4). It shows that increase the value of Mixed convection parameter decease velocity curve; it is expected to existence of buoyancy forces. A reverse relation between Nr and $f'(\eta)$ is obtained by Fig. (5), an increment in values of Nr as a result decreases the curve of velocity component $f'(\eta)$ same impact shows for Nc and porosity K are delegated in figures (6-7). Fig. 8 illustrates the change of thermophoresis parameter Nt on temperature distribution. The figure depicts that $\theta(\eta)$ is the increasing functions of thermophoresis parameter for some growing values of Nt. The increasing value of Nt results to raises the thermal conductivity of liquid. The heavy-duty thermal conductivity liquid comprises advanced temperature field $\theta(\eta)$. In thermophoresis, tiny particles of fluid are dragged from hot surface to cold. Thus, caused by departure of many tiny particles from hot surface temperature rises. Fig. 9 indicates the conduct of temperature profile with respect to parametric values of diffusivity ratio *Nb*. When a gradual increment is done in the morals of diffusivity ratio *Nb*, deceleration is obtained in the temperature function. Fig. 9 shows the consequence of shrinking parameter λ on temperature profile. The decrease in the principles of λ in the stretching case resulted in reducing the temperature contour $\theta(\eta)$. Figure (10-11) describes the prominence of porosity parameter K and heat generation/absorption parameter on temperature field $\theta(\eta)$.

The enhancement in K and Δ results in much convective heat transfer and concentration rate. Henceforth rise in the distribution for temperature of fluid. Temperature distribution of nanoparticles is enhanced because of the high temperature. The influence of Prandtl number on temperature field $\theta(\eta)$ illustrated in figure (12). Temperature of nanoparticles drop because of enhancement in $\Pr$. Prandtl number is termed as ratio among thermal conductivity of fluid and thermal diffusivity of a fluid. In consequence, minimum value of Prandtl number consequences in the maximum thermal diffusivity while this causes lesser boundary layer thickness and temperature. Figure (13) demonstrates the impact of thermal radiation Rd on temperature field. These figures depict that $\theta(\eta)$ is the increasing functions of radiation parameter for some growing values of Rd. Fig. 14 displays the effect of stretching or shrinking sheet parameter on concentration profile. On increasing values of λ, a decreasing behavior of concentration is obtained. The Impact of chemical diffusion on concentration profile is shown on Figures (15). The curve of concentration distribution is increased as value of γ increased.

Figure (16) illustrates the influence of thermophoresis parameter Nt on concentration field. These figures depict that $\phi(\eta)$ is the increasing functions of thermophoresis parameter for some growing values of Nt. The increasing value of Nt results to raises the thermal conductivity of liquid. The heavy-duty thermal conductivity liquid comprises advanced concentration profile $\phi(\eta)$. In thermophoresis, tiny particles of fluid are dragged from hot surface to cold. Thus, caused by departure of many tiny particles from hot surface temperature rises and this high temperature points to an increment in the concentration. The concentration profile grows faster and once a minor change, it falloffs. The description for significance of Brownian motion parameter Nb on temperature field of nanoparticles is explored in Figure (17). In Fig. (18), diffusivity ratio parameter *Nb* is depicted to show its behavior on concentration profile. A significant downfall in the curve of concentration profile is obtained when gradual increase is done in diffusivity ratio parameter *Nb.* The Impact of Le on concentration profile is shown on figures (19). The curve of concentration distribution is increased as value of Le increased. Fig (20) denotes the consequences of parameter E called energy activation parameter on concentration profile $\phi(\eta)$. By enhancing the values of E concentration profile boosted up. Fig (21) represents the effects of parameter σ called microorganism concentration difference on density profile $\chi(\eta)$. By enhancing the values of σ density profile retarded. From Figure (22), it is demonstrated that within the increment in bio-convection Peclet number Pe, the density $\chi(\eta)$ is

retarded. Here the extreme rapidity of cell-swimming is enriched by raise the value of Pe. This advanced rapidity of cell-swimming is accountable in the lesser performance of $\chi(\eta)$. The graph of Schmidt number *Sc* on motile density field is displayed in Fig. 23. Density function of motile microorganisms is decreased for gradual increase in Schmidt number.

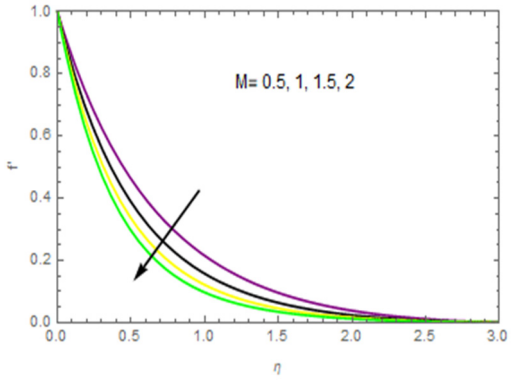

Figure 1. Influence of M on velocity field

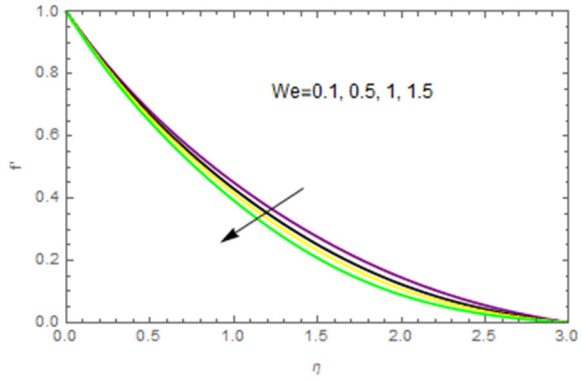

Figure 2. Inspiration of We on velocity variable

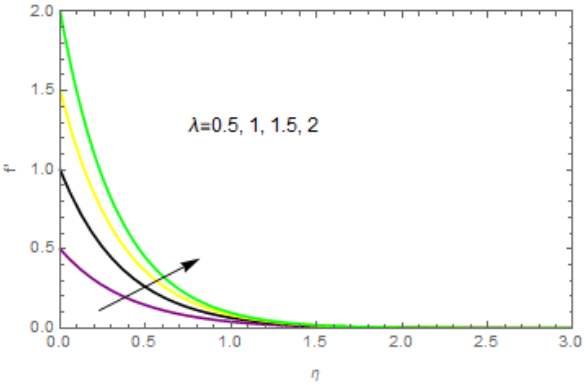

Figure 3. Effect of Stretching parameter on velocity function

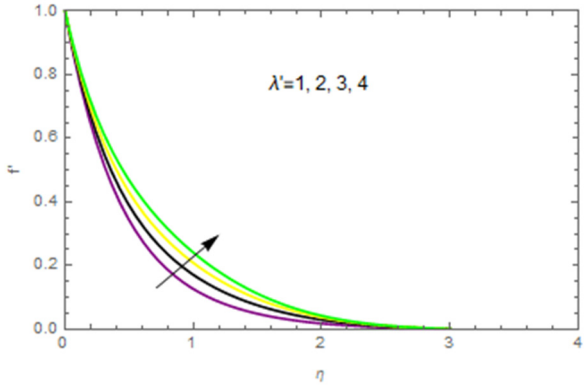

Figure 4. Impact of Mixed convection Parameter on velocity Distribution

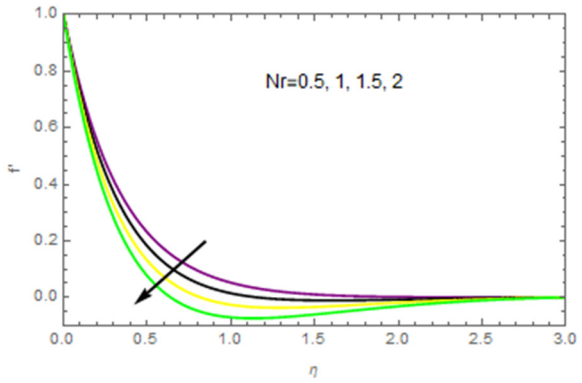

Figure 5. Change of Nr on velocity Distribution

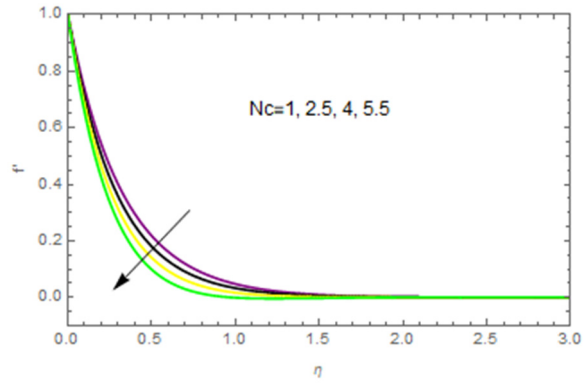

Figure 6. Change of Nc on velocity Distribution

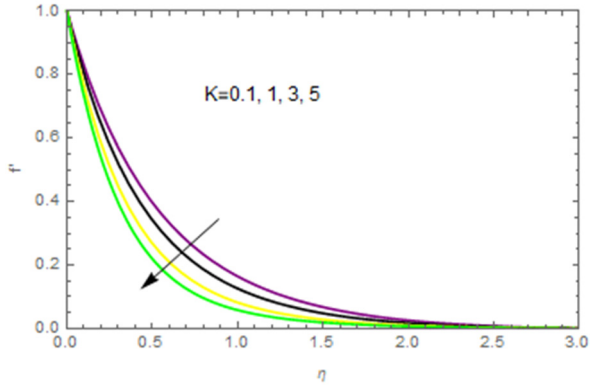

Figure 7. Influence of K on velocity Distribution

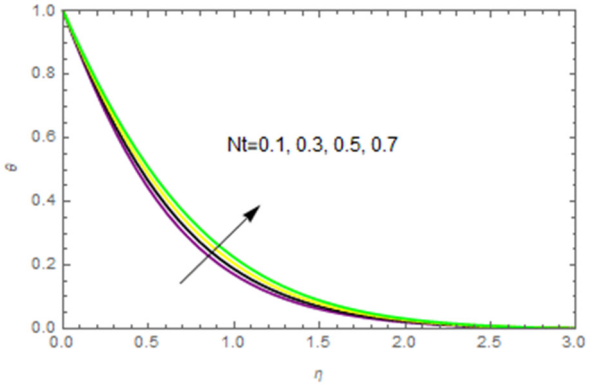

Figure 8. Influence of Nt on Energy Distribution

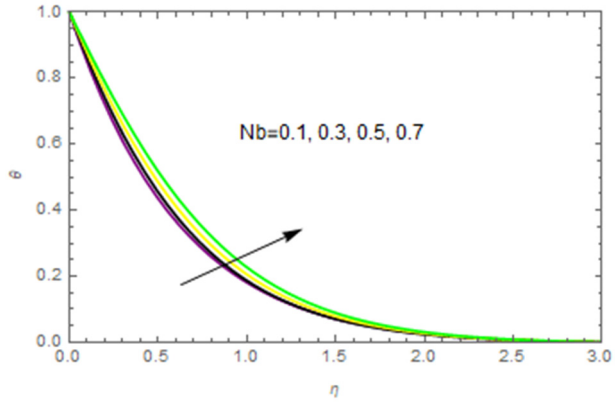

Figure 9. Change of Nb on Energy Distribution

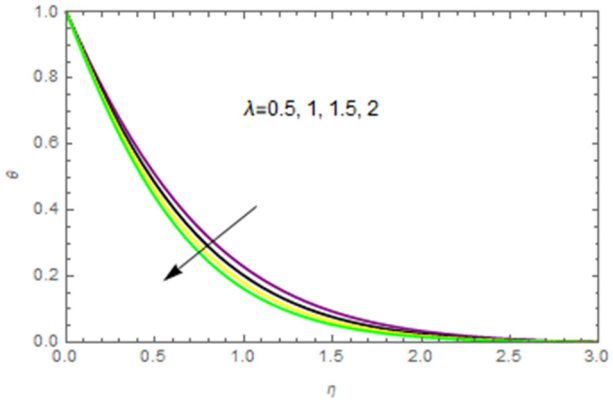

Figure 10. Impact of stretching parameter on Energy field

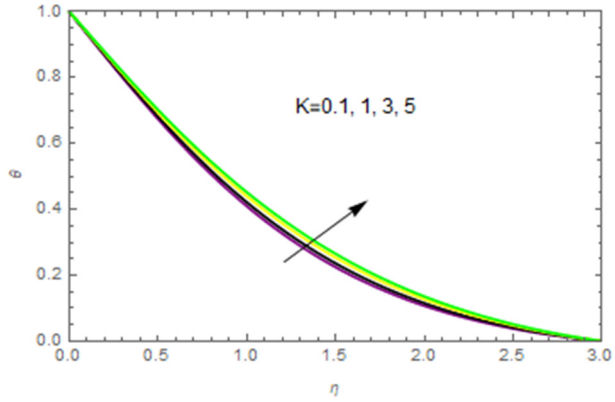

Figure 11. Influence of permeable parameter on Energy field

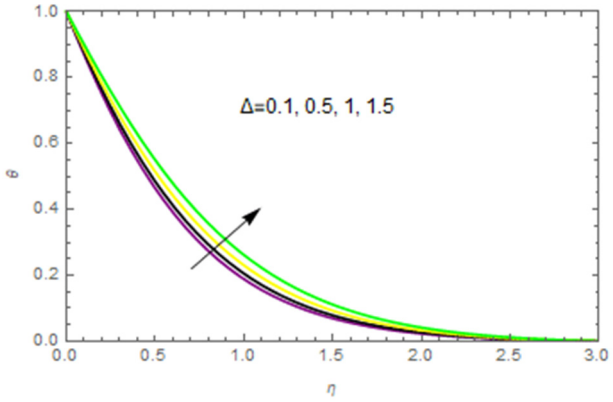

Figure 12. variation of Heat on Energy Distribution

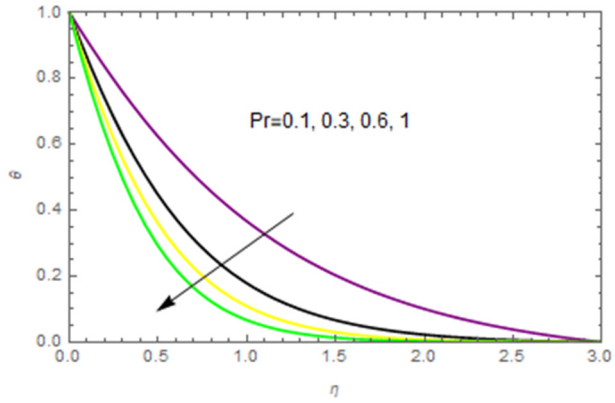

Figure 13. variation of Pr on Energy profile

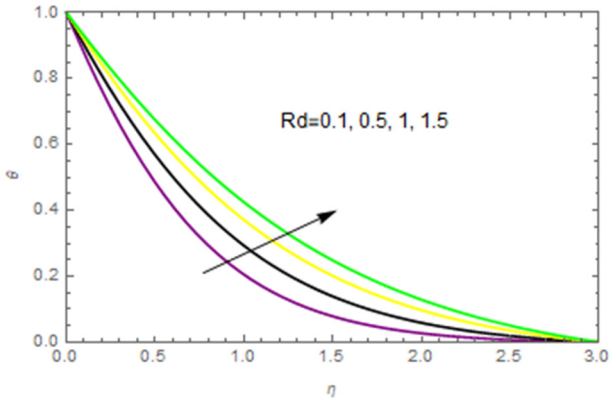

Figure 14. Influence of Rd on Energy function

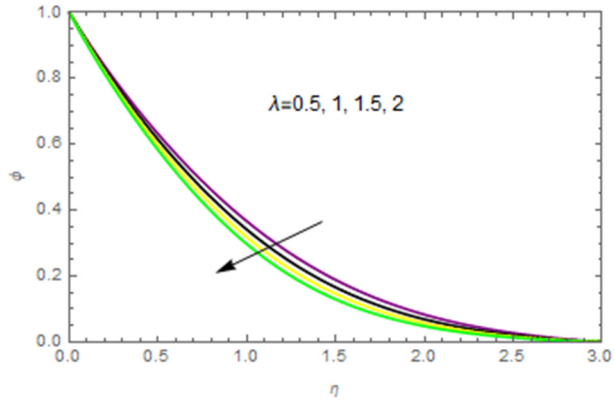

Figure 15. Impact of stretching parameter on Concentration Distribution

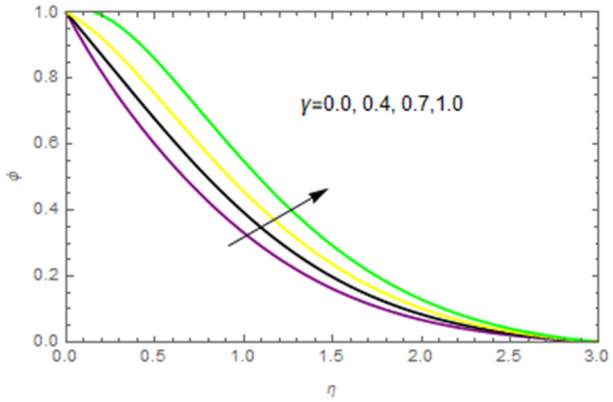

Figure 16. Influence of Chemical Reaction on Concentration Distribution

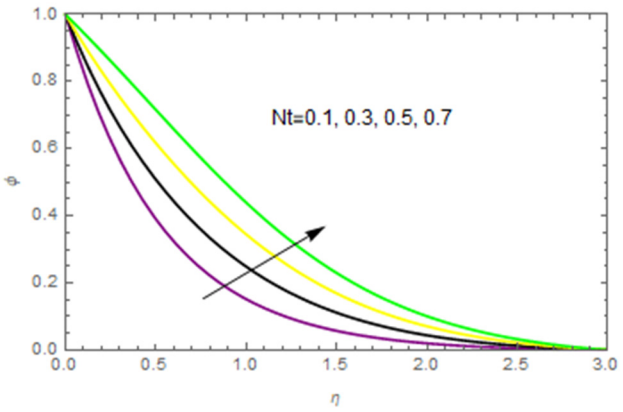

Figure 17. Influence of Nt on Concentration variable

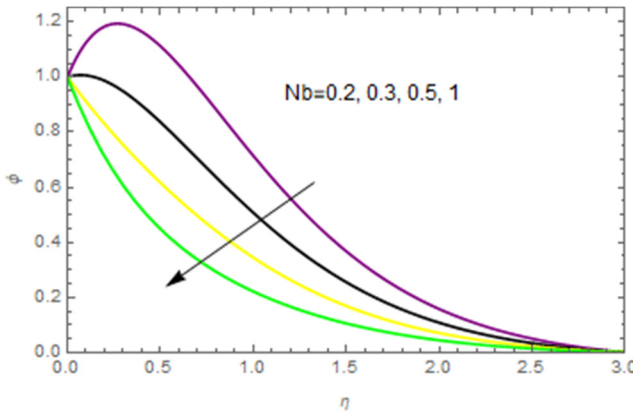

Figure 18. Variation of Nb on Concentration field

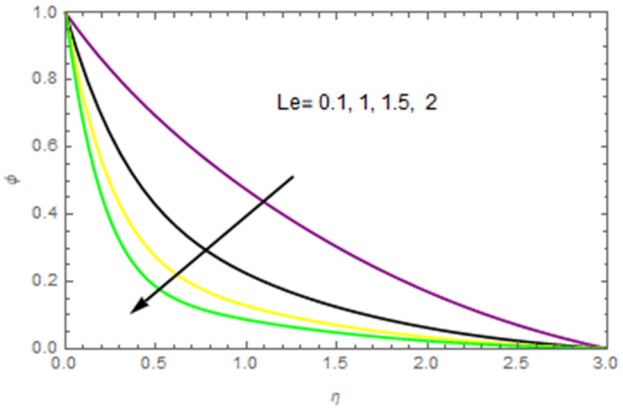

Figure 19. Influence of Le on Concentration Distribution

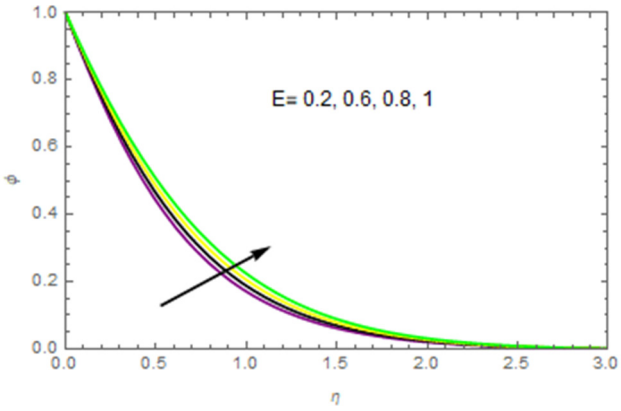

Figure 20. Influence of E on Concentration field

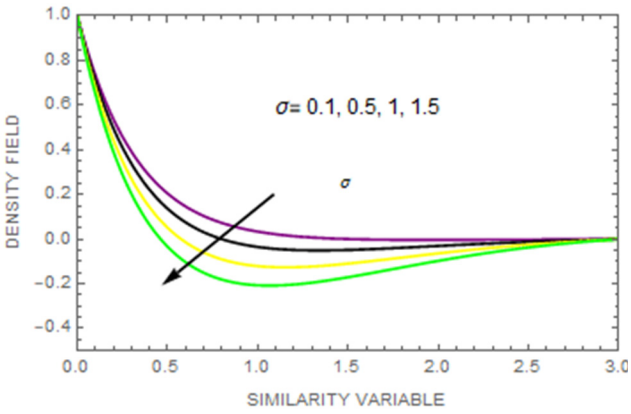

Figure 21. Influence of Microorganism rotation on Density field

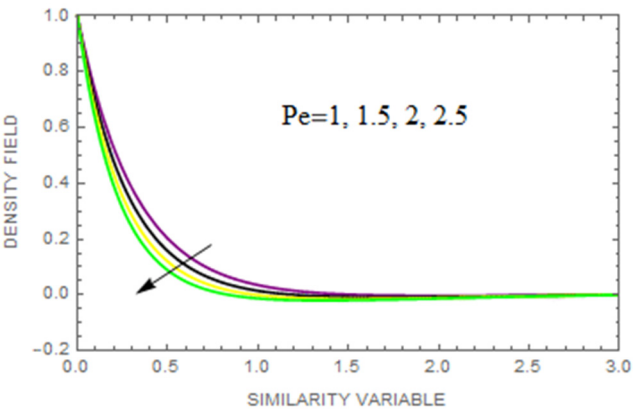

Figure 22. Variation of Pe on Density field

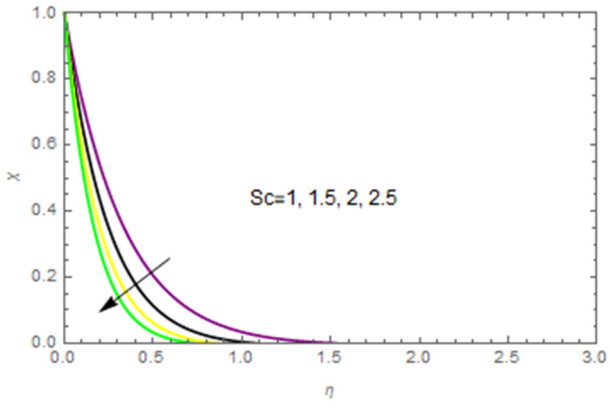

Figure 23. Influence of Sc on Density Distribution

Table 2. Nusselt number, local Sherwood number and density number at the stretching walls using ND solve command in Mathematica.

M	λ	σ	Pe	S	Pr	Nb	Nc	γ	Le	Sc	$Nu_x Re_x^{-\frac{1}{2}}$	$Sh_x Re_x^{-\frac{1}{2}}$	$Nn_x Re_x^{-\frac{1}{2}}$
	0.3	0.2	2.0	1	1.0	0.3	0.3	0.1	0.4	0.4	1.16659	0.56552	4.32923
1.0													
2.0											1.15123	0.40950	3.21537
3.0											1.07338	0.16075	1.04172
	0.2										0.17512	0.45780	2.94381
	0.6										0.17228	0.44645	2.85185
	0.8										0.16902	0.41387	2.74916
		0.5									1.13333	0.40568	1.36869
		0.9									1.13333	0.40570	1.41039
		1.3									1.13333	0.40570	1.45210
			1.0								1.13733	0.22030	0.43075
			1.5								1.13733	0.22030	0.47950
			2.0								1.13733	0.22030	0.52876
				1							2.16131	1.43887	4.26398
				2							2.16042	1.43678	4.24719
				3							2.15951	1.43469	4.22999
					1.0						0.45077	0.00966	-0.74797
					2.0						0.68383	-0.08266	-1.23763
					3.0						0.84725	-0.07903	-1.04744
						1					1.15746	0.43021	3.19426
						2					0.82402	0.90844	7.04756
						3					0.56577	1.04348	8.14001
							0.5				1.15742	0.43021	3.19438
							1				0.95049	0.10051	0.67048
							1.5				0.86338	0.02481	0.16697
								0.1			1.15752	0.43031	3.19430
								0.5			1.05198	0.48546	3.63174
								1.0			0.99724	0.51466	3.86424
									0.5		1.08467	0.35129	2.43540
									1.0		0.93459	0.66762	5.01487
									1.5		0.83409	0.97854	7.05759
										1	0.82405	0.90852	7.04755
										2	0.89141	0.75773	5.85983
										3	0.92656	0.68164	5.26339

CONCLUSION

The major findings are given below:

- The flow speed distribution improves with mixed convection parameter λ'. and diminishes with Harman number M .
- Energy distribution increased for thermophoresis Nt, Brownian motion parameters Nb and radiation parameter Rd.
- Concentration enhanced with activation energy E, thermal radiation Rd and buoyancy ratio number Nr.
- The motile microorganism distribution and recced with Picklet number Pe, bio convection Lewis number Le and Schmidt number Sc and increased with bioconvection Rayleigh number.

Conflict of Interest: None

ORCID IDs

Muhammad Jawad, https://orcid.org/0000-0002-9304-615X

REFERENCES

[1] S. Maripala, and N. Kishan, "Unsteady MHD flow and heat transfer of nanofluid over a permeable shrinking sheet with thermal radiation and chemical reaction", American Journal of Engineering Research, **4**(6), 68–79 (2015).

[2] C.R. Reddy, and R.R. Kairi, "The effect of melting on mixed convection heat and mass transfer in non-Newtonian nanofluid SATURATEED in porous medium", Frontiers in Heat and Mass Transfer, **6**, 6 (2015). http://www.thermalfluidscentral.com/journals/index.php/Heat_Mass_Transfer/article/view/408/402

[3] L.G. Vijaya, B.L. Anand, and R.K. Srinivasa, "MHD mixed convection stagnation point flow of nanofluid through a porous medium over stretching sheet," International Journal of Pure and Applied Mathematics, **118**(10), 369-389 (2018). https://acadpubl.eu/jsi/2018-118-10-11/articles/10/38.pdf

[4] N. Ambreen, A. Rehman, N. Sheikh, S. Iqbal, and M. Zulfiqar, "Boundary-layer flow and heat transfer over a rotating porous disk in a non-Newtonian Williamson nanofluid", Indian Journal of Science and Technology, **12**(38), (2019). https://doi.org/10.17485/ijst/2019/v12i38/146120

[5] Aurangzaib, A.R.M. Kasim, N.F. Mohammad, and S, Shafie, "Unsteady MHD mixed convection flow with heat and mass transfer over a vertical plate in a micropolar fluid-saturated porous medium", Journal of Applied Science and Engineering, **16**(2), 141-150 (2013). https://doi.org/10.6180/jase.2013.16.2.05

[6] G.B. Reddy, B.S. Goud, and M.N.R. Shekar, "Numerical solution of MHD mixed convective boundary layer flow of a nanofluid through a porous medium due to an exponentially stretching sheet with magnetic field effect", International Journal of Applied Engineering Research, **14**(9), 2074-2083 (2019). https://www.ripublication.com/ijaer19/ijaerv14n9_01.pdf
[7] A. Al-Mamun, S.M. Arifuzzaman, S. Reza-E-Rabbi, P. Biswas, and M. Khan, "Computational Modelling on MHD radiative Sisko nanofluids flow through a nonlinearly stretching sheet", International Journal of Heat and Technology, **37**(1), 285-295 (2019). https://doi.org/10.18280/ijht.370134
[8] S.E. Ahmed, R.A. Mohamed, A.E.M. Aly, and M.S. Soliman, "Magnetohydrodynamic Maxwell nanofluids flow over a stretching surface through a porous medium", International Journal of Mechanical, Industrial and Aerospace Sciences, **13**(6), (2019).
[9] S.U. Choi, and J.A. Eastman, *Enhancing thermal conductivity of fluids with nanoparticles*, Argonne National Lab. IL (United States), Tech. Rep. (1995).
[10] S.K. Das, S.U. Choi, W. Yu, and T. Pradeep, *Nanofluids: science and technology*, (John Wiley & Sons, 2007).
[11] R.V. Williamson, "The flow of pseudoplastic materials," Industrial and Engineering Chemistry, **21**(11), 1108-1111 (1929). https://doi.org/10.1021/ie50239a035
[12] M. Y. Malik, M. Bibi, F. Khan, and T. Salahuddin, "Numerical solution of Williamson fluid flow past a stretching cylinder and heat transfer with variable thermal conductivity and heat generation/absorption", AIP Advances, **6**(3), 035101 (2016). https://doi.org/10.1063/1.4943398
[13] M. R. Krishnamurthy, B.C. Prasannakumara, B.J. Gireesha, and R.S.R. Gorla, "Effect of chemical reaction on MHD boundary layerflow and melting heat transfer of Williamson nanofluid in porous medium", Engineering Science and Technology, an International Journal, **19**(1), 53-61 (2016). http://dx.doi.org/10.1016/j.jestch.2015.06.010
[14] S. Nadeem, S.T. Hussain, and C. Lee, "Flow of a Williamson fluid over a stretching sheet", Brazilian Journal of Chemical Engineering, **30**(3), 619-625 (2013). https://doi.org/10.1590/S0104-66322013000300019
[15] M.J. Babu, and N. Sandeep, "MHD non-Newtonian fluid flow over a slandering stretching sheet in the presence of crossdiffusion effects", Alexandria Engineering Journal, **55**(3), 2193-2201 (2016). https://doi.org/10.1016/j.aej.2016.06.009
[16] M.S. Khan, M.M. Rahman, S.M. Arifuzzaman, P. Biswas, and I. Karim, "Williamson fluid flow behaviour of MHD convective radiative Cattaneo-Christov heat flux type over a linearly stretched-surface with heat generation and thermal-diffusion", Frontiers in Heat and Mass Transfer, **9**(15), 1 (2017). https://nova.newcastle.edu.au/vital/access/manager/Repository/uon:32963
[17] A.R. Bestman, "Natural convection boundary layer with suction and mass transfer in a porous medium", International Journal of Energy Research, 14(4), 389-396 (1990). https://doi.org/10.1002/er.4440140403
[18] A. Hamid, Hashim, and M. Khan, "Impacts of binary chemical reaction with activation energy on unsteady flow of magneto Williamson nanofluid", Journal of Molecular Liquids, **262**, 435-442 (2018). https://doi.org/10.1016/j.molliq.2018.04.095
[19] S. Anuradha, and K. Sasikala, "MHD free convective flow of a nanofluid over a permeable shrinking sheet with binary chemical reaction and activation energy", International Journal of Engineering Science Invention, **7**(1), 22-30 (2018).
[20] M. Dhlamini, P.K. Kameswaran, P. Sibanda, S. Motsa, and H. Mondal, "Activation energy and binary chemical reaction effects in mixed convective nanofluid flow with convective boundary conditions", Journal of Computational Design and Engineering, **6**(2), 149-158 (2019). https://doi.org/10.1016/j.jcde.2018.07.002
[21] F.G. Awad, S. Motsa, and M. Khumalo, "Heat and mass transfer in unsteady rotating fluid flow with binary chemical reaction and activation energy", PLoS One, **9**(9), e107622 (2014). https://doi.org/10.1371/journal.pone.0107622
[22] M. Mustafa, J.A. Khan, T. Hayat, and A. Alsaedi, "Buoyancy effects on the MHD nanofluid flow past a vertical surface with chemical reaction and activation energy", International Journal of Heat and Mass Transfer, **108**, 1340-1346 (2017). https://doi.org/10.1016/j.ijheatmasstransfer.2017.01.029
[23] C.-J. Huang, "Arrhenius activation energy effects on free convective about a permeable horizontal cylinder in porous medium", Transport in Porous Media, **128**, 723-740 (2019). https://doi.org/10.1007/s11242-019-01267-1
[24] A. Zaib, M.M. Rashidi, A. Chamkha, and K. Bhattacharyya, "Numerical solution of second law analysis for MHD Casson nanofluid past a wedge with activation energy and binary chemical reaction", International Journal of Numerical Methods for Heat & Fluid Flow, **27**(12), 2816-2834 (2017). https://doi.org/10.1108/HFF-02-2017-0063
[25] M. Monica, J. Sucharitha, and C.H. Kishore, "Effects of exothermic chemical reaction with Arrhenius activation energy, non-uniform heat source/sink on MHD stagnation point flow of a Casson fluid over a nonlinear stretching sheet with variable fluid properties and slip conditions", Journal of the Nigerian Mathematical Society, **36**, 163-190 (2017). https://ojs.ictp.it/jnms/index.php/jnms/article/view/93/27
[26] T. Hayat, I. Ullah, M. Waqas, and A. Alsaedi, "Attributes of activation energy and exponential based heat source in flow of Carreau fluid with cross-diffusion effects," Journal of Non-Equilibrium Thermodynamics, **44**(2), 203-213 (2019). https://doi.org/10.1515/jnet-2018-0049
[27] Z. Shafique, M. Mustafa, and A. Mushtaq, "Boundary layer flow of Maxwell fluid in rotating frame with binary chemical reaction and activation energy," Results in Physics, **6**, 627-633 (2016). https://doi.org/10.1016/j.rinp.2016.09.006
[28] A.M. Spormann, "Unusual swimming behavior of a magnetotactic bacterium", FEMS Microbiol. Ecol. **3**(1), 37-45 (1987). https://doi.org/10.1111/j.1574-6968.1987.tb02336.x
[29] A. Raees, H. Xu, S.-J. Liao, "Unsteady mixed nanobioconvection flow in a horizontal channel with its upper plate expanding or contracting", Int. J. Heat Mass Transf. **86**, 174-182 (2015). https://doi.org/10.1016/j.ijheatmasstransfer.2015.03.003
[30] S. Siddiqa, N. Begum, S. Saleem, M. Hossain, R.S.R. Gorla, "Numerical solutions of nanofluid bioconvection due to gyrotactic microorganisms along a vertical wavy cone", Int. J. Heat Mass Transf. **101**, 608-613 (2016). https://doi.org/10.1016/j.ijheatmasstransfer.2016.05.076
[31] A. Abbasi, F. Mabood, W. Farooq, and M. Batool, "Bioconvective flow of viscoelastic nanofluid over a convective rotating stretching disk", Int. Commun. Heat Mass Transfer, **119**, 104921 (2020). https://doi.org/10.1016/j.icheatmasstransfer.2020.104921
[32] Y.-M. Chu, M.I. Khan, N.B. Khan, S. Kadry, S.U. Khan, I. Tlili, and M. Nayak, "Significance of activation energy, bioconvection and magnetohydrodynamic in flow of third grade fluid (non-newtonian) towards stretched surface: A buongiorno model analysis", Int. Commun. Heat Mass Transfer, **118**, 104893 (2020). https://doi.org/10.1016/j.icheatmasstransfer.2020.104893

[33] O. Makinde, and I. Animasaun, "Bioconvection in MHD nanofluid flow with nonlinear thermal radiation and quartic autocatalysis chemical reaction past an upper surface of a paraboloid of revolution", Int. J. Therm. Sci. **109**, 159-171 (2016). https://doi.org/10.1016/j.ijthermalsci.2016.06.003

[34] M.B. Henda, H. Waqas, M. Hussain, S.U. Khan, W. Chammam, S.A. Khan, and I. Tlili, "Applications of activation energy along with thermal and exponential space-based heat source in bioconvection assessment of magnetized third grade nanofluid over stretched cylinder/sheet", Case Studies in Thermal Engineering, 101043, (2021). https://doi.org/10.1016/j.csite.2021.101043

[35] S. Hussain, M.R. Sharma, M.R. Mishra, and S.S. Alrashidy, "Hydromagnetic dissipative and radiative graphene Maxwell nanofuid fow past a stretched sheet-numerical and statistical analysis", Mathematics, **8**, 1929 (2020). https://doi.org/10.3390/math8111929

[36] I. Dapra, and G. Scarpi, "Perturbation solution for pulsatile fow of a non-Newtonian Williamson fluid in a rock fracture", Int. J. Rock Mech. Mining Sci. **44**, 271-278 (2007). https://doi.org/10.3390/w12051341

ВПЛИВ ЕНЕРГІЇ АРРЕНІУСА ТА СОНЯЧНОГО ВИПРОМІНЮВАННЯ НА ЕЛЕКТРОПРОВІДНІСТЬ НАНОРІДИНИ ВІЛЬЯМСОНА З ПЛАВАЮЧИМ МІКРООРГАНІЗМОМ: ЗАВЕРШЕННЯ МОДЕЛІ БУОНДЖОРНО

Мухаммад Джавад

Департамент математики, Фейсалабадський університет, Файсалабад 38000, Пакистан

Збагачені термічні механізми та прогресивність наноматеріалів спонукали вчених присвятити себе цій галузі в наші дні. Універсальне та синтезуюче використання таких частинок охоплює виробництво енергії, сонячні системи, процеси моніторингу опалення та охолодження, системи відновлюваної енергії, лікування раку, гібридні двигуни та наноелектроніку. Крім того, в цю еру біотехнології та біоінженерії біоконвекція нанорідин забезпечує деякі захоплюючі застосування, такі як ферменти, біосенсори та біопаливо. Представлено математичну модель для оцінки електропровідності нанорідини Вільямсона з тепло- та масообміном через пористий розтягнутий лист за наявності біоконвекції. Біоконвекція плаваючих мікроорганізмів, теплове випромінювання, теплопровідність і енергія Арреніуса є новими аспектами цього дослідження. Нелінійні керуючі диференціальні рівняння з частинними похідними (PDE) вищого порядку розв'язуються шляхом застосування відповідних змінних подібності, і в результаті створюється пара звичайних диференціальних рівнянь (ODE). Розроблений набір ODE розв'язується чисельно за допомогою добре відомої техніки зйомки за допомогою команди ND solve у Wolfram MATHEMATICA та порівнюється з результатом коду pvb4c у MATLAB. Отримані графіки для різних фізичних величин, що представляють інтерес, разом із безрозмірними профілями швидкості, температури, концентрації та щільності мікроорганізмів для включення таких параметрів, як магнітний параметр, броунівський рух, число Релея, число Пекле, біоконвективне число Льюїса, параметр термофорезу і параметра коефіцієнта плавучості. Обговорюється вплив численних параметрів на характеристики потоку та теплообміну.

Ключові слова: *енергія активації; нанорідини Вільямсона; хімічна реакція; теплове випромінювання; метод стрільби; лист, що розширюється; теплопровідність*

East European Journal of Physics. 1. 146-153 (2023)
DOI:10.26565/2312-4334-2023-1-18 ISSN 2312-4334

STRUCTURAL, ELECTRICAL AND OPTICAL STUDIES OF $Ni_xCd_{1-x}S$ (x = 0.8, 0.6, 0.4 and 0.2) NANOPARTICLE SYSTEM†

Moly M. Rose[a,*], R. Sheela Christy[a], T. Asenath Benitta[a], J. Thampi Thanka Kumaran[b]
[a]*Department of Physics and Research Centre (Reg.No.18123112132030), Nesamony Memorial Christian College, Marthandam, Affiliated to Manonmaniam Sundaranar University, Abishekapatti, Tirunelveli, Tamil Nadu, India*
[b]*Department of Physics and Research Centre, Malankara Catholic College Mariagiri*
**Corresponding Author e-mail: molyrengith@gmail.com*
Received January 23, 2023; revised January 28, 2023; accepted February 3, 2023

This paper demonstrates the synthesis of $Ni_xCd_{1-x}S$ (x=0.8,0.6,0.4,0.2) nanoparticles by microwave-assisted chemical precipitation method. The prepared samples were characterized by XRD, EDAX, SEM, UV-VIS, and PL spectroscopy. The energy-dispersive x-ray analysis confirms the existence of Nickel, Cadmium and Sulphur in proper ratios. The DC electrical resistances were measured in the temperature range of 300 K-500 K. The temperature resistance curves of all the samples show phase transitions above a particular temperature. The UV and PL spectra of all the samples were compared and studied.
Keywords: *nanoparticles; chemical precipitation; phase transition; electrical; optical; bandgap*
PACS: 81.07.-b, 05.70.-a, 81.20.Fw, 61.05.C-, 78.20.-e, 68.37.-d, 81.07.-b, 88.40.H-, 87.64.Ee

1. INTRODUCTION

Nickel Sulphide Nanoparticles are important members of the transition metal sulphide nanomaterials, which also include Ni_3S_2, Ni_4S_3, Ni_6S_5, Ni_7S_6, Ni_9S_8, Ni_3S_4, and NiS [1]. Nickel Sulphide nanoparticles have attracted much interest because of their novel physical, optical, and electrical properties [2]. Nickel Sulphide nanoparticles have potential applications in rechargeable lithium batteries [3, 4], solar cells [5, 6], catalyst devices [7, 8], and image processing devices [9, 10]. Due to the variety of applications, different synthesis methods, such as the solvothermal method [7], the sonochemical method [8], the hydrothermal method [9], and microwave irradiation [10], were used to prepare the NiS nanoparticles.

Cadmium Sulphide (CdS) is an important II-VI semiconductor with a direct band gap of 2.4 eV at room temperature and many excellent physical and chemical properties [11]. Due to its wide band gap, it has been used in many applications such as field effect transistors [12], solar cells [13], light-emitting diodes [14], photocatalysis [15], photographic developers [16], and biological sensors [17]. Various methods have been used to synthesize CdS nanoparticles, such as sol-gel [18], aqueous precipitation [19], hydrothermal [20], sonochemical [21], and microwave heating [22].

Phase transitions in Nickel Sulphide nanoparticles were already studied by varying the thermal annealing temperature [23]. Phase transitions in Cadmium Sulphide nanoparticles have already been reported by varying pressure, modifying the bath temperature, and varying annealing temperatures [24–30]. Ni_xCd_{1-x} S (x = 0.8,0.6,0.4 and 0.2) nanoparticles have both the applications of Nickel Sulphide nanoparticles and Cadmium Sulphide nanoparticles. M. Elango and D. Nataraj studied synthesis and characterization of Nickel doped Cadmium Sulphide ($CdS:Ni^{2+}$) nanoparticles[31]. D. Wu and F. Wang synthesized NiS/CdS nanocomposite by hydrothermal process and studied their photocatalytic performance [32]. Photocatalytic Activity of Pure and Nickel Doped Cadmium Sulphide Nanoparticles were synthesized by co-Precipitation Method [33].

In the present study, we synthesized $Ni_xCd_{1-x}S$ (x= 0.8,0.6,0.4 and 0.2) nanoparticles by microwave assisted chemical precipitation and studied their phase transition through DC electrical resistance measurements at various temperatures. When compared to conventional heating, microwave irradiation can shorten the reaction time. The optical properties of the samples were compared using the UV and PL spectra of the samples.

2. EXPERIMENTAL DETAILS

2.1. Synthesis of $Ni_xCd_{1-x}S$ (x= 0.8,0.6,0.4 and 0.2) nanoparticles by microwave assisted chemical precipitation method

$Ni_xCd_{1-x}S$ (x = 0.8, 0.6, 0.4, and 0.2) nanoparticles were created using Nickel acetate, Cadmium acetate, and Sodium Sulphide. Separately, Nickel acetate and Cadmium acetate were dissolved in 20 ml of distilled water and then mixed together. The Sodium Sulphide solution obtained by dissolving 6.14 g of Sodium Sulphide in 40 ml of distilled water was added in drops to the above solution after effective stirring for 3 hours and kept undisturbed for one day. After complete precipitation, the precipitates were filtered out separately, washed thoroughly with deionized water several times, and kept in a microwaveoven. The solution was then subjected to microwave irradiation of 800 W for 20 minutes for efficient heating. The nanoparticles thus obtained were then cooled to room temperature. Finally, the nanoparticles were annealed at 100^0C for one hour to get the pure $Ni_xCd_{1-x}S$ (x = 0.8, 0.6, 0.4, and 0.2) nanoparticles. The collected $Ni_xCd_{1-x}S$

† ***Cite as:*** M.M. Rose, R.S. Christy, T.A. Benitta, and J.T.T. Kumaran, East Eur. J. Phys. **1**, 146 (2023), https://doi.org/10.26565/2312-4334-2023-1-18

(x = 0.8, 0.6, 0.4, and 0.2) nanoparticles were used for various characterizations. Table 1 shows the amount of precursor materials used to dissolve in 40 ml of distilled water.

Table 1. The amount of precursor materials taken to dissolve in 40 ml distilled water.

Sl no	Composition	Nickel acetate	Cadmium acetate
1	$Ni_{0.8}Cd_{0.2}S$	3.91gm	1.06gm
2	$Ni_{0.6}Cd_{0.4}S$	2.93gm	2.13gm
3	$Ni_{0.4}Cd_{0.6}S$	1.95gm	3.19gm
4	$Ni_{0.2}Cd_{0.8}S$	0.9gm	4.26gm

2.2. Instrumentation

X-ray diffraction (XRD) patterns of the synthesized sample were recorded on a powder X-ray diffractometer with Cu Kα radiation (λ = 1.54 Å) with 2θ ranging from angles 10°- 80°. The surface morphology of the samples has been studied using a TESCAN VEGA3 SBH scanning electron microscope. The elemental compositions were identified using an energy dispersed X-ray analysis setup attached to the scanning electron microscope. The optical absorption spectra of the synthesized nanoparticles were recorded on a UV-visible spectrometer in the wave length range of 200–900 nm. Photoluminescence measurements were performed on a Varian Cary Eclipse photoluminescence spectrophotometer in the range 300-650 nm. A compressed collection of nanoparticles (pellets) was obtained by applying a high pressure of 10 tons/cm^2**.** The resistance of the pellet form of the samples was measured using a four-probe technique.

3. RESULT AND DISCUSSION

Figure 1 shows the XRD patterns of $Ni_xCd_{1-x}S$ (x = 0.8, 0.6, 0.4, and 0.2) nanoparticles synthesized by microwave-assisted chemical precipitation method. The respective EDAX images shown in Figure 2 confirm their compositions.

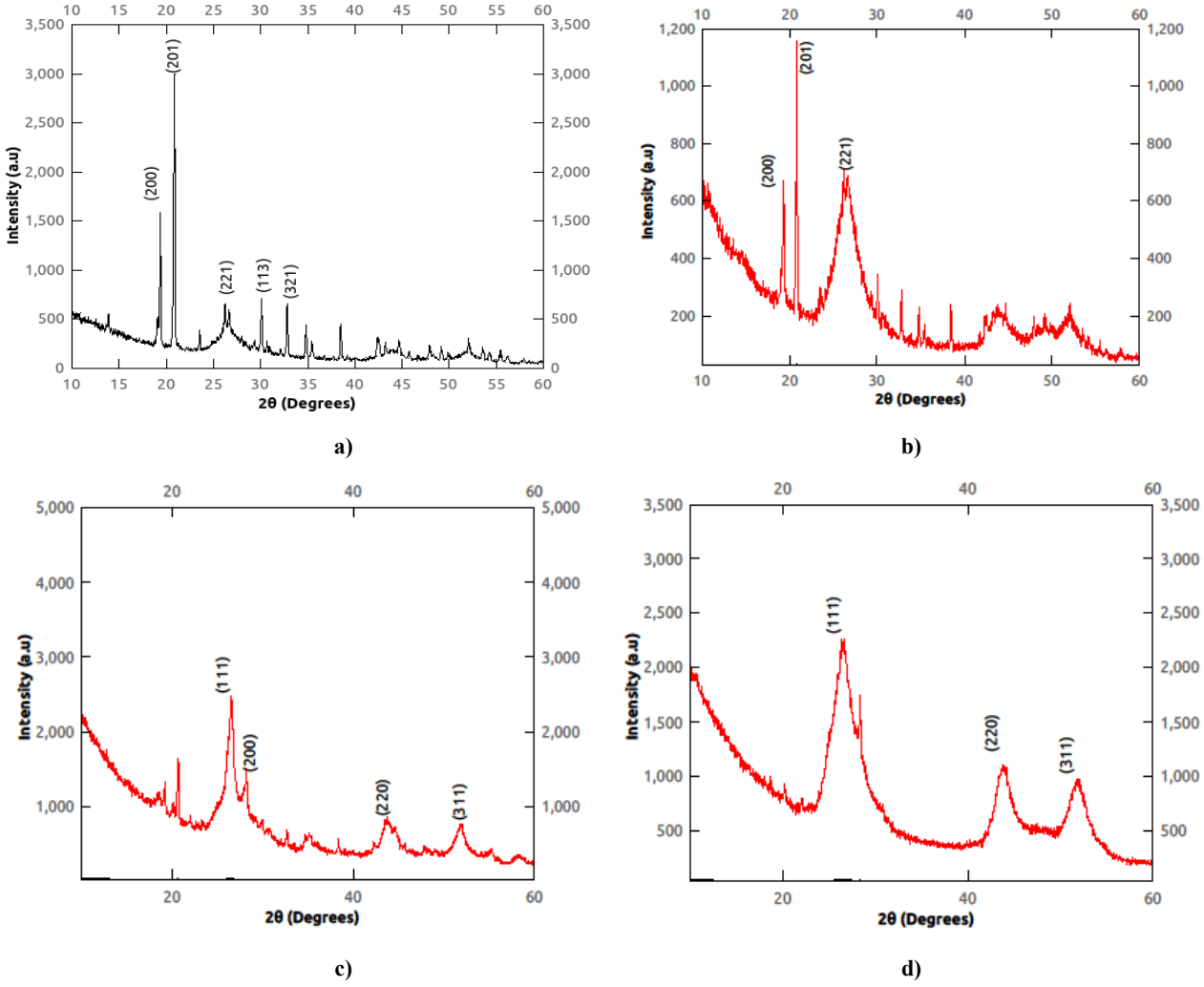

Figure 1. Indexed XRD patterns of $Ni_xCd_{1-x}S$ nanoparticles
a) $Ni_{0.8}Cd_{0.2}S$ nanoparticles, b) $Ni_{0.6}Cd_{0.4}S$ nanoparticles, c) $Ni_{0.4}Cd_{0.6}S$ nanoparticles, d) $Ni_{0.2}Cd_{0.8}S$ nanoparticles

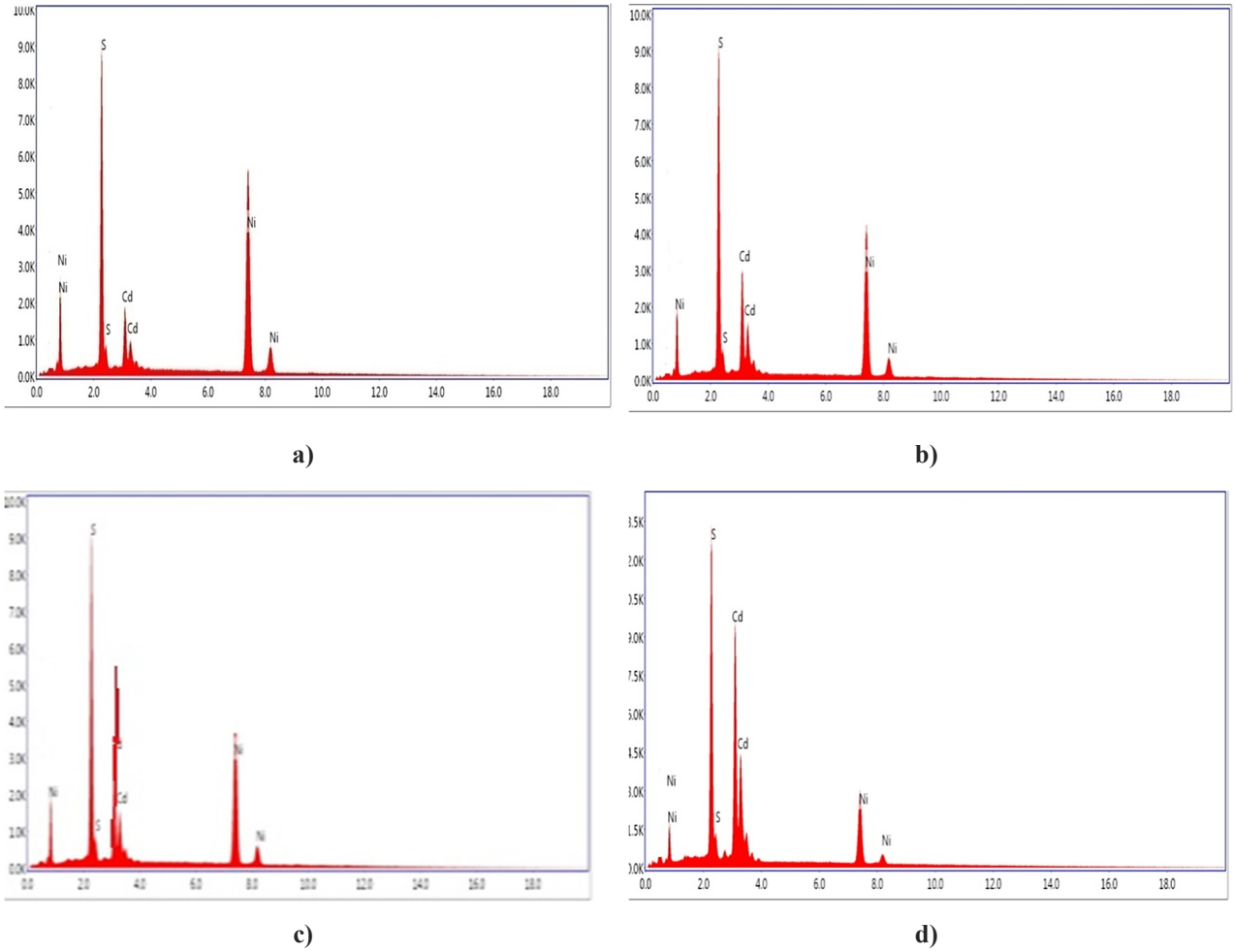

Figure 2. EDAX images of $Ni_xCd_{1-x}S$ nanoparticles
a) $Ni_{0.8}Cd_{0.2}S$ nanoparticles, b) $Ni_{0.6}Cd_{0.4}S$ nanoparticles, c) $Ni_{0.4}Cd_{0.6}S$ nanoparticles, d) $Ni_{0.2}Cd_{0.8}S$ nanoparticles

Figure 3 shows the SEM images of synthesized $Ni_xCd_{1-x}S$ (x = 0.8, 0.6, 0.4, and 0.2). SEM images show the uniform distribution of nanoparticles. Table 2 gives the composition, structure at room temperature, lattice parameters, and particle size of the synthesized samples. As the composition of Cd increases, the particle size decreases. The mixture at room temperature reveals the structure of any one of its components [34,35]. Structural studies clearly indicates that by suitably adjusting the composition, the nanoparticles can be synthesized with either orthorhombic phase or cubic phases and with desired particle size.

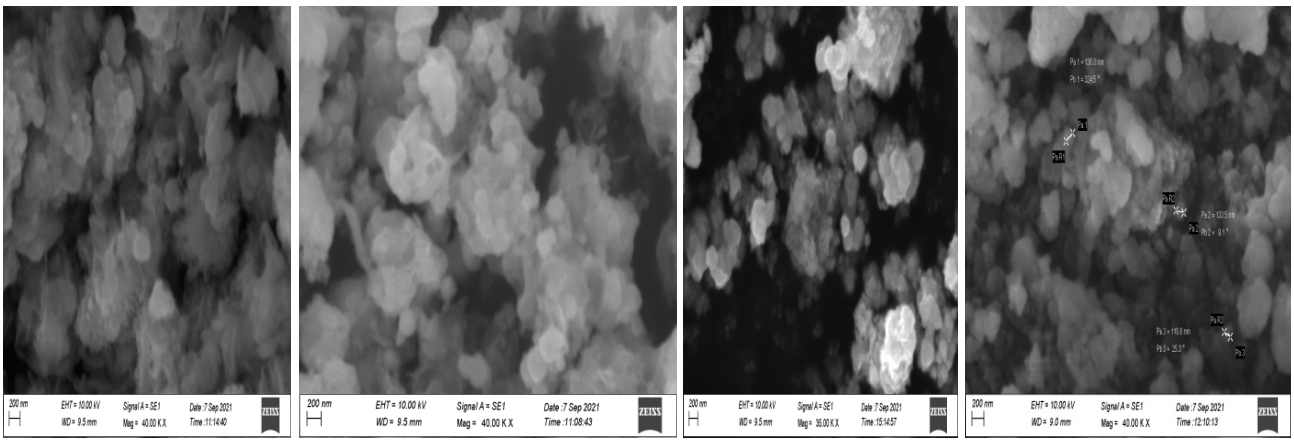

Figure 3. SEM images of synthesized $Ni_xCd_{1-x}S$ nanoparticles
a) $Ni_{0.8}Cd_{0.2}S$ nanoparticles, b) $Ni_{0.6}Cd_{0.4}S$ nanoparticles c) $Ni_{0.4}Cd_{0.6}S$ nanoparticles d) $Ni_{0.2}Cd_{0.8}S$ nanoparticles

Table2. The samples, structure at room temperature, particle size and lattice constants of $Ni_xCd_{1-x}S$ (X= 0.8,0.6,0.4,0.2) nanoparticles

The samples	Structure at room temperature	Particle size	Lattice constants
$Ni_{0.8}Cd_{0.2}S$ nanoparticles	Orthorhombic structure	44nm	a=9.29Å, b=11.12Å, c=9.39Å
$Ni_{0.6}Cd_{0.4}S$ nanoparticles	Orthorhombic structure	37nm	a=9.20, b=11.10Å, c=9.29Å
$Ni_{0.4}Cd_{0.6}S$ nanoparticles	Cubic structure	14nm	a=b=c=5.8Å
$Ni_{0.2}Cd_{0.8}S$ nanoparticles	Cubic structure	5nm	a=b=c=5.68Å

3.1. Electrical studies of $Ni_xCd_{1-x}S$ (x = 0.8, 0.6, 0.4, 0.2) nanoparticles synthesized by microwave-assisted chemical precipitation method

Resistance variations with temperature of $Ni_xCd_{1-x}S$ (x = 0.8, 0.6, 0.4, and 0.2) nanoparticles (300K-500K) are shown in Figure 4 respectively. Table.3 lists the compositions, their behaviour at room temperature, order of resistance, possible transition temperatures, and their behaviour after phase transition. By varying the composition of Nickel and Cadmium, it is possible to synthesize nanoparticles with the desired resistance and electrical behavior. The electrical properties of the sample can also be changed according to the table by increasing the temperature. This change in electrical property is due to phase transition [36].

Table 3. Composition, behavior of the sample at room temperature, order of resistance, possible transition temperatures, behavior of the sample after phase transition of $Ni_xCd_{1-x}S$(x = 0.8, 0.6, 0.4, 0.2) nanoparticles

Sl.NO	Compositions	Behaviour of the sample at room temperature	Order of resistance	Possible transition temperatures	Behaviour of the sample after phase transition
1	**$Ni_{0.8}Cd_{0.2}S$**	Semiconductor	10^8 Ohm	>353K	Conductor
2	**$Ni_{0.6}Cd_{0.4}S$**	insulator	10^9 Ohm	>353K	Semiconductor
3	**$Ni_{0.4}Cd_{0.6}S$**	Semiconductor	10^6 Ohm	>373K	Insulator
4	**$Ni_{0.2}Cd_{0.8}S$**	Semiconductor	10^6 Ohm	>363K	Insulator

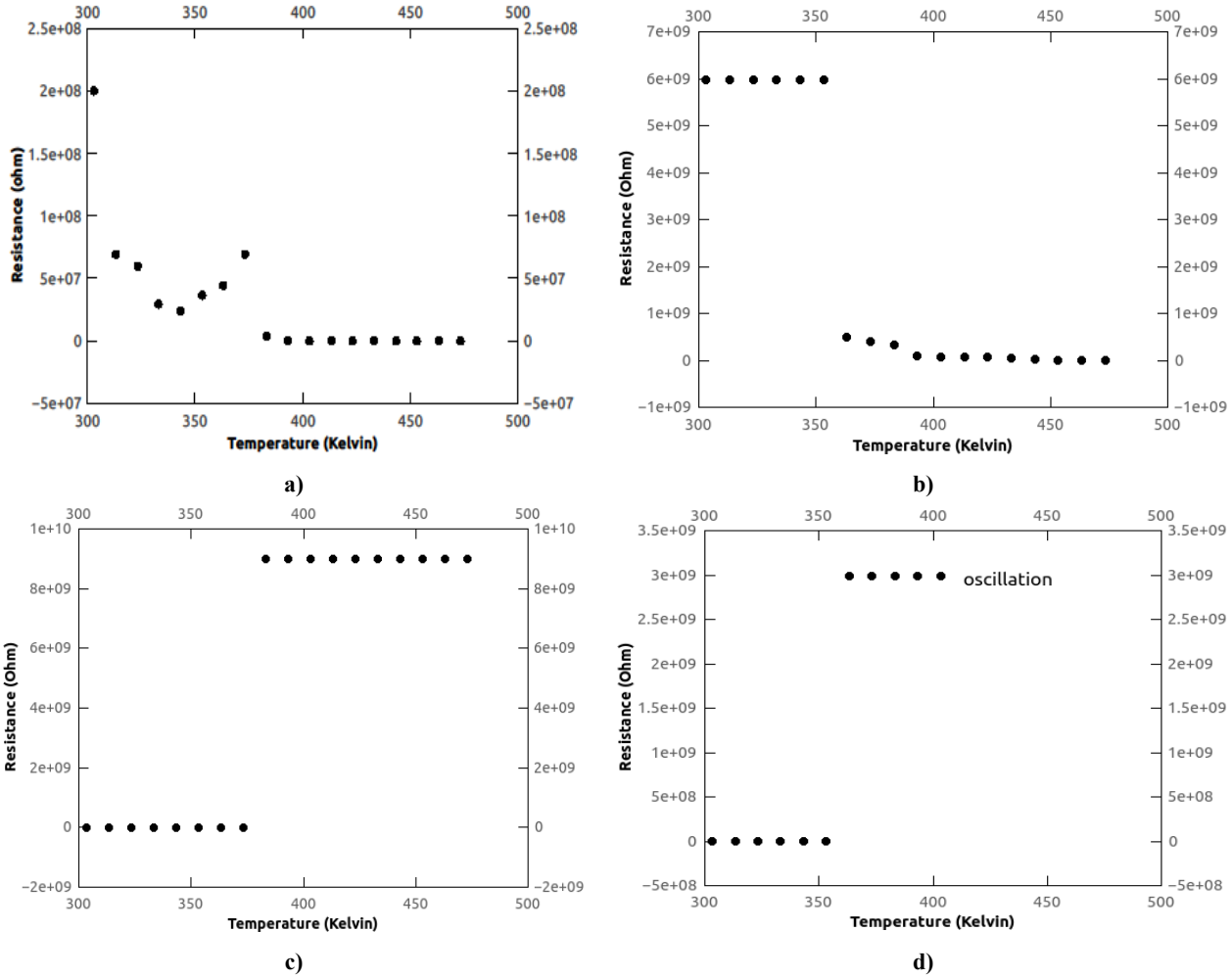

Figure 4. Variation of resistance with temperature of $Ni_xCd_{1-x}S$ nanoparticles
a) $Ni_{0.8}Cd_{0.2}S$, b) $Ni_{0.6}Cd_{0.4}S$, c) $Ni_{0.4}Cd_{0.6}S$, d) $Ni_{0.2}Cd_{0.8}S$

3.2. Optical studies of $Ni_xCd_{1-x}S$ (x = 0.8, 0.6, 0.4, 0.2) nanoparticles synthesized by microwave-assisted chemical precipitation method

UV studies. The optical absorption spectra of $Ni_xCd_{1-x}S$ (x = 0.8, 0.6, 0.4, and 0.2) nanoparticles are shown in Figure 5. The optical absorption spectrum of $Ni_{0.8}Cd_{0.2}S$ nanoparticles shows one more absorption edge near 900nm (Fig. 5a). As more and more Cd is incorporated, this absorption edge goes on decreasing and disappears in the $Ni_{0.2}Cd_{0.8}S$ nanoparticles mixture.

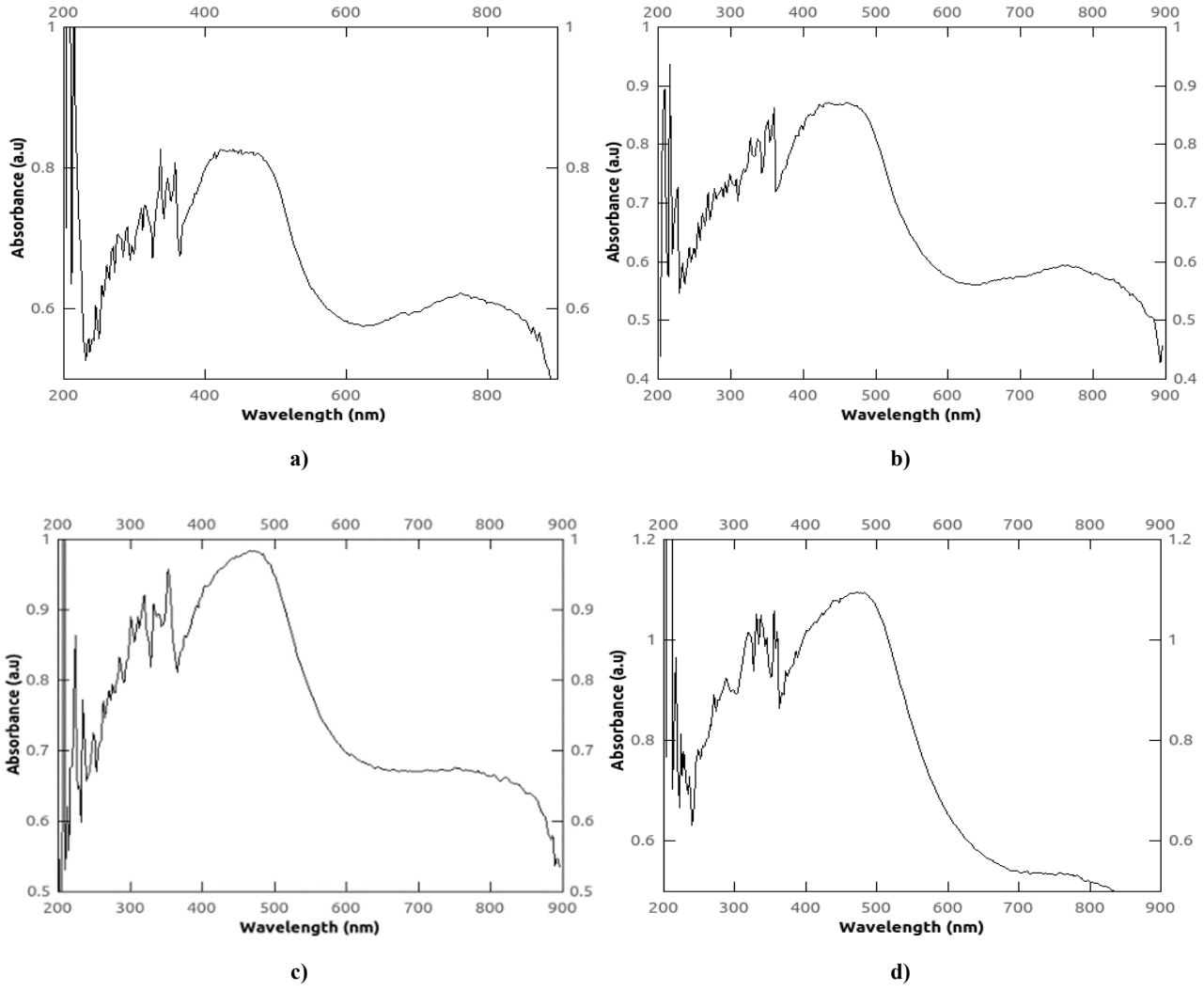

Figure 5. Optical absorption Spectrum of $Ni_xCd_{1-x}S$ nanoparticles
a) $Ni_{0.8}Cd_{0.2}S$ nanoparticles, b) of $Ni_{0.6}Cd_{0.4}S$ nanoparticles, c) $Ni_{0.4}Cd_{0.6}S$ nanoparticles, d) $Ni_{0.2}Cd_{0.8}S$ nanoparticles

The tauc's plots of $Ni_xCd_{1-x}S$ (x = 0.8, 0.6, 0.4, and 0.2) nanoparticles are shown in Figure 6. By replacing 20% of Ni by Cd in the NiS nanoparticles the bandgap energy shifts from 3.5 eV to 2.2 eV, ie the bandgap energy of CdS [37]. Hence by incorporating Cd in NiS nanoparticles the bandgap energy can be reduced to a large extent, and also the absorption shifts from UV to visible region. Hence it can be used as light-sensitive materials. The compositions and bandgap energy of $Ni_xCd_{1-x}S$ (x = 0.8, 0.6, 0.4, and 0.2) nanoparticles are tabulated in Table 4. When more Cd is incorporated, the band gap decreases.

Table4. The sample, bandgap of $Ni_xCd_{1-x}S$ (x = 0.8, 0.6, 0.4,0.2) nanoparticles

Samples	Bandgap
$Ni_{0.8}Cd_{0.2}$ S	2 eV
$Ni_{0.6}Cd_{0.4c}S$	1.9 eV
$Ni_{0.4}Cd_{0.6c}S$	1.85 eV
$Ni_{0.2}Cd_{0.8}$ S	1.8 eV

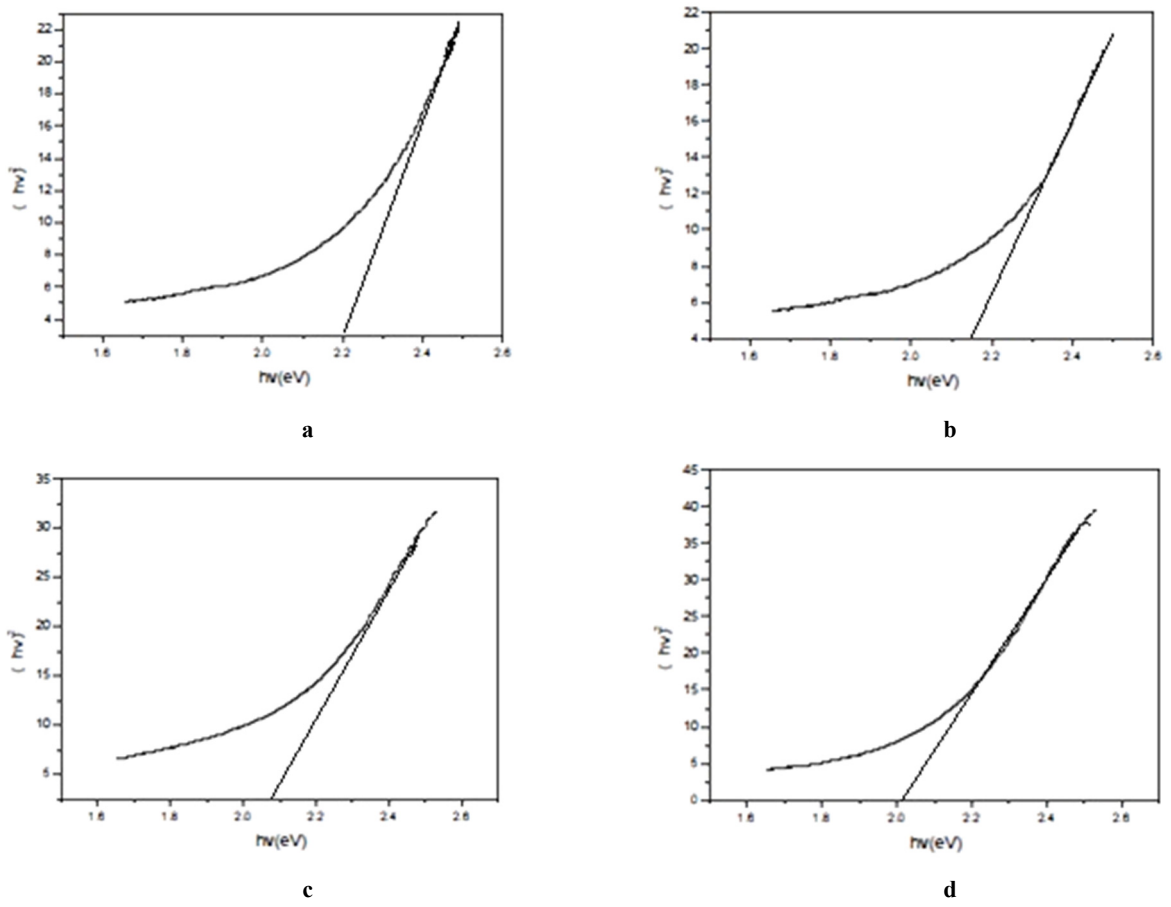

Figure 6. Tauc's plot of $Ni_xCd_{1-x}S$ nanoparticles
a) $Ni_{0.8}Cd_{0.2}S$ nanoparticles, b) of $Ni_{0.6}Cd_{0.4}S$ nanoparticles, c) $Ni_{0.4}Cd_{0.6}S$ nanoparticles, d) $Ni_{0.2}Cd_{0.8}S$ nanoparticles

PL Studies. The PL emission spectra of $Ni_xCd_{1-x}S$ nanoparticles (x = 0.8, 0.6, 0.4, and 0.2) are shown in Figure 7. As the composition of Cd increases, the emission spectrum shifts towards the higher wavelength, i.e., towards the emission wavelength of pure CdS [38]. From the luminous spectroscopy (Figure 7), it has been found that the emission peak shifts from 440 nm to 470 nm (close to the emission peak of CdS) [39]. when more Cd is incorporated. Figure 8 depicts the variation of peak positions with composition of $Ni_xCd_{1-x}S$ nanoparticles (x = 0.8, 0.6, 0.4, and 0.2). Because this variation is linear, $Ni_xCd_{1-x}S$(x = 0.8, 0.6, 0.4, and 0.2) nanoparticles can be tuned to emit different wavelengths in the range 440 nm – 470 nm by varying the Cd composition, and the sample composition can also be identified from the graph by observing the emission peak.

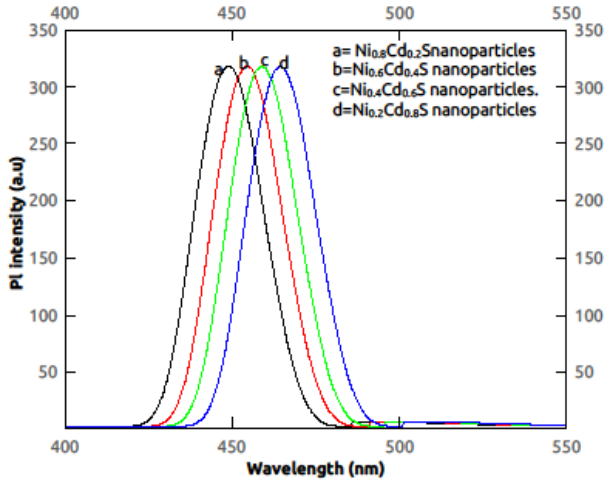

Figure 7. Pl emission spectra of $Ni_xCd_{1-x}S$ (x = 0.8,0.6,0.4,0.2) nanoparticles

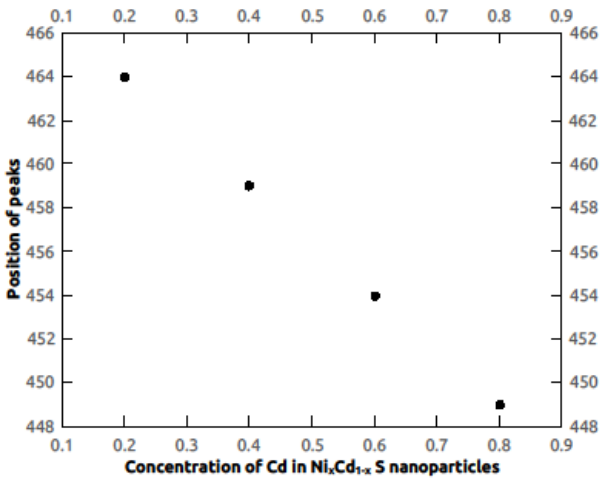

Figure 8. The variation of position of peaks with composition of $Ni_xCd_{1-x}S$ (x = 0.8,0.6,0.4,0.2) nanoparticles

4. CONCLUSION

We successfully synthesized $Ni_xCd_{1-x}S$ (x = 0.8, 0.6, 0.4, and 0.2) nanoparticles using microwave-assisted chemical precipitation, and the nanoparticles were characterized using XRD, SEM, and EDAX analyses. The DC electrical resistances were measured in the temperature range 300 K-500 K. All the samples undergo phase transition above a particular temperature. The behaviour of the samples at room temperature is entirely different from the behaviour of the samples after phase transition. From the absorption spectroscopy, it is clear that when the concentration of Cd is increased, the bandgap energy decreases. $Ni_xCd_{1-x}S$ (x = 0.8, 0.6, 0.4, and 0.2) nanoparticles can be tuned to emit different wavelengths in the range 440 nm–470 nm by varying the Cd composition, and the sample composition can also be identified from the graph by observing the emission peak.

Acknowledgements

The authors gratefully acknowledge Nesamony Memorial Christian College, Marthandam, for providing the necessary laboratory facilities to carry out this work.

Funding. This study was done towards the Ph.D. work of Mrs. Moly M. Rose and was not funded by any external agencies.
Competing Interests. We have not received any funding from any company or university, and hence, there is no conflict of interest.
Author Contributions. All authors discussed the results and contributed to the final manuscript.
Data availability statement. The data that support the findings of this study are available within the article

ORCID IDs

Moly M. Rose, https://orcid.org/0000-0003-4840-0567

REFERENCES

[1] P.-F. Yin, L.L. Sun, C. Zhou, Y.-H. Sun, X.Y. Han, and C.R. Deng, "Synthesis, characterization and magnetic property of 3D flower-like Nickel Sulphide nanocrystals through decomposing bis(thiourea) nickel(II) chloride crystals", Bull. Mater. Sci. **38**(1), 2015, 95 (2014). https://doi.org/10.1007/s12034-014-0815-6

[2] S. Darezereshki, A.B. Vakylabad, A. Hassanzadeh, T. Niedoba, A. Surowiak, and B. Koohestani, "Hydrometallurgical Synthesis of Nickel Nano-Sulfides from Spent Lithium-Ion Batteries", Minerals, **11**, 419 (2021). https://doi.org/10.3390/min11040419

[3] E. Darezereshki, A.B. Vakylabad, A. Hassanzadeh, T. Niedoba, A. Surowiak, and B. Koohestani, "Hydrometallurgical Synthesis of Nickel Nano-Sulfides from Spent Lithium-Ion Batteries", Minerals, **11**, 419 (2021). https://doi.org/10.3390/min11040419

[4] A. Sarkar, A.K. Chakraborty, and S. Bera, "NiS/rGO nanohybrid: An excellent counter electrode for dye sensitized solar cell", Solar Energy Materials and Solar Cells, **182**, 314 (2018). https://doi.org/10.1016/j.solmat.2018.03.026

[5] I.M. Maafa, "Synthesis and characterization of NiS Nanoparticles Carbon Nanofiber Composite as Electrocatalyst for Methanol Oxidation", Int. J. Electrochem. Sci. **16**, 210431 (2021). https://doi.org/10.20964/2021.04.32

[6] S. Nagaveena, S.N. Kumar, and C.K. Mahadevan, "Synthesis by a Novel Method and Application of Image Processing in Characterization of Nickel Sulphide Nanoparticles", International Journal of Engineering Research and Applications, **3**(2), 1214 (2013). https://www.academia.edu/download/31091547/GP3212141218.pdf

[7] R. Bhardwaj, R. Jha, M. Bhushana, and R. Sharma, "Enhanced electrocatalytic activity of the solvothermally synthesized Mesoporous Rhombohedral Nickel Sulphide", Materials Science in Semiconductor Processing, **118**(1), 105194 (2020). https://doi.org/10.1016/j.mssp.2020.105194

[8] M. Kristl, B. Dojer, S. Gyergyek, and J. Kristl, "Synthesis of nickel and cobalt sulfide nanoparticles using a low cost sonochemical method", Heliyon 3, e00273 (2017). http://dx.doi.org/10.1016/j.heliyon.2017.e00273

[9] B. Naresh, D. Punnoose, S.S. Rao, A. Subramnian, B.R. Ramesh, and H.-J. Kim, "Hydrothermal synthesis and pseudocapacitivve properties of morphology-tuned nickel sulfide (NiS) nanostructures", New Journal of Chemistry, **4**, (2018). https://doi.org/10.1039/C7NJ05054B

[10] H. Banaiean-Monfared, H. Emadi, and M. Enhessari, "Synthesis and characterization of nickel sulfide nanoparticles via cyclic microwave radiation", Comptes Rendus Chimie, **16**(10), 929936 (2013). https://doi.org/10.1016/j.crci.2013.01.011

[11] V. Singh, P.K. Sharma, P. Chauhana, "Surfactant mediated phase transformation of CdS nanoparticles," Mater. chemistry physics, **121**, 202-207 (2010). https://doi.org/10.1016/j.matchemphys.2010.01.019

[12] R.-M. Ma, L. Dai, H.-B. Huo, W.-J. Xu, and G.G. Qin, "High-Performance Logic Circuits Constructed on Single CdS Nanowires," Nanoletters, **7**(11), 3300 (2007). https://doi.org/10.1021/nl071528

[13] C. Martınez-Alonso, H.J. Cortina-Marrero, C.S. Coria-Monroy, M.C. Arenas, M.E. Nicho, and H. Hu, "Solution synthesized CdS nanoparticles for hybrid solar cell Applications," J. Mater. Sci: Mater Electron. **26**, 5539 (2015). https://doi.org/10.1007/s10854-014-2072-2

[14] M. Kowshik, N. Deshmukh, W. Vogel, J. Urban, S.K. Kulkarni, and K.M. Panikar, "Microbial Synthesis of semiconductor CdS Nanoparticles, Their Characterization, and Their Use in the Fabrication of an ideal diode", Biotechnology and Bioengineering, **78**(5), 583 (2002). https://doi.org/10.1002/bit.10233

[15] D. Ayodhya, M. Venkatsham, A. Santhoshikumari, G. Bhagavanthreddy, and G. Veerabhadram "One Spot Sonochemical Synthesis of CdS nanoparticles: Photocatalytic and electrical properties", Int. J. Ind. Chem, 6, 261-271 (2015). https://doi.org/10.1007/s40090-015-0047-7

[16] Q. Wu, L. Huang, Z. Li, W. An, D. Liu, J. Lin, L. Tian, et al., "The Potential Application of Raw Cadmium Sulfide Nanoparticles as CT Photographic Developer", Nanoscale Research Letters, **11**, 232 (2016). https://doi.org/10.1186/s11671-016-1424-7

[17] R. Harish, K.D. Nisha, S. Prabakaran, B. Sridevi, S. Harish, M. Navaneethan, S. Ponnusamy, et al., "Cytotoxicity assessment of chitosan coated CdS nanoparticles for bio-imaging applications", Applied Surface Science, **499**, 143817 (2020). https://doi.org/10.1016/j.apsusc.2019.143817

[18] N.V. Hullavarad, and S.S. Hullavarad, "Synthesis and characterization of monodispersed CdS nanoparticles in SiO_2 fibers by sol-gel method", Photonics and Nanostructures Fundamentals and Applications, **5**, 156 (2007). https://doi.org/10.1016/j.photonics.2007.03.001

[19] P. Rodriguez, N. Munoz-Aguirre, E. San-Martin Martinez, G. Gonzalez de la Cruz, S.A. Tomas, and O.Z. Angel, "Synthesis and spectral properties of starch capped CdS nanoparticles in aqueous solution", Journal of Crystal Growth, **310**, 160 (2008). https://doi.org/10.1016/j.jcrysgro.2007.09.036
[20] R. Xu, Y. Wanga, G. Jia, W. Xu, S. Liang, and D. Yin, "Zinc blende and wurtzite cadmium sulfide nanocrystals with strong photoluminescence and ultrastability", Journal of Crystal Growth, **299**, 28 (2007). https://doi.org/10.1016/j.jcrysgro.2006.11.252
[21] V.P. Singh, R.S. Singh, G.W. Thompson, V. Jayaraman, S. Sanagapalli, and V.K. Rangari, "Characteristics of nanocrystalline CdS films fabricated by sonochemical, microwave and solution growth methods for solar cell applications," Solar Energy Materials & Solar Cells, **81**, 293 (2004). https://doi.org/10.1016/j.solmat.2003.11.007
[22] Y. Wada, H. Kuramoto J. Anand, T. Kitamura, T. Sakata, H. Mori, and S.J. Yanagida, "Microwave-assisted size control of CdS nanocrystallites", Mater. Chem. **11**, 1936 (2001). https://doi.org/10.1039/b101358k
[23] O.O. Balayeva, A.A. Azizov, M.B. Muradov, A.M. Maharramov, G.M. Eyvazova, R.J. Gasimov, and Z.X. Dadashov, "Effect of thermal annealing on the properties of nickel sulfide nanostructures: Structural phase transition", Materials Science in Semiconductor Processing, **64**, 130 (2017). https://doi.org/10.1016/j.mssp.2017.03.021
[24] P. Wang, B. Xiao, R. Zhao, Y. Ma, and M. Zhang, "Structure-Dependent Spin Polarization in Polymorphic CdS:Y Semiconductor Nanocrystals", ACS Applied Materials & Interfaces, https://doi.org/10.1021/acsami.5b12542
[25] R. Martın-Rodrıguez, J. Gonzalez, R. Valiente, F. Aguado D. Santamarıa-Perez, and F. Rodrıguez, "Reversibility of the zinc-blende to rock-salt phase transition in cadmium sulfide nanocrystals", Journal of applied physics, **111**, 063516 (2012). http://dx.doi.org/10.1063/1.3697562
[26] X. Li, H. Zhang, J. Gao, D. Guo, C. Yang, L. Xu, B. Liu, et al., "Transition temperature reduction for CdS nanoparticles under high pressure", J. Nanopart. Res. **13**, 6563 (2011). https://doi.org/10.1007/s11051-011-0562-1
[27] L. Meng, J.M.D. Lane, L. Baca, J. Tafoya, T. Ao, B. Stoltzfus, et al., "Shape Dependence of Pressure-Induced Phase Transition in CdS Semiconductor Nanocrystals", J. Am. Chem. Soc. **142**, 6505 (2020). https://dx.doi.org/10.1021/jacs.0c01906
[28] J. Marquez-Marin, C.G. Torres-Castanedo, G. Torres-Delgado, M.A. Aguilar-Frutis, R. Castanedo-Perez, and O. Zelaya-Angel, "Very sharp zinc blende-wurtzite phase transition of CdS nanoparticles", Superlattices and Microstructures, **102**, 442 (2017). https://doi.org/10.1016/j.spmi.2017.01
[29] V. Sivasubramanian, A.K. Arora, M. Premila, C.S. Sundar, and V.S. Sastry, "Optical properties of CdS nanoparticles upon annealing", Physica E: Low-dimensional Systems and Nanostructures, **31**, 93 (2006). https://doi.org/10.1016/j.physe.2005.10.001
[30] M.M. Rose, R.S. Christy, T.A. Benitta, and J.T.T. Kumaran, "Phase transitions in cadmium sulfide nanoparticles", AIP Advances **11**, 085129 (2021). https://doi.org/10.1063/5.0052078
[31] M. Elango, D. Nataraj, K.P. Nazeer, and M. Thamilselvan, "Synthesis and characterization of nickel doped cadmium sulfide ($CdS:Ni^{2+}$) nanoparticles", Materials Research Bulletin, **47**(6), 1533 (2016). https://doi.org/10.1016/j.materresbull.2012.02.033
[32] D. Wu, F. Wang, Y. Tan, and C. Li, "Facile synthesis of NiS/CdS nanocomposites for photocatalytic degradation of quinoline under visible-light irradiation", RSC Adv. **6**, 73522 (2016). https://doi.org/10.1039/C6RA13439D
[33] A.M.B. Leena, and K. Raji, "Photocatalytic Activity of Pure and Nickel Doped Cadmium Sulphide Nanoparticles Synthesized via Co-Precipitation Method", J. Nanosci. Tech. **5**(3), 710 (2019). https://doi.org/10.30799/jnst.S21.19050301
[34] V.P.M. Shajudheen, V.S. Kumar, K.A. Rani, M. Uma, and K. Saravana, "Structural and Optical Properties of NiS Nanoparticles Synthesized by Chemical Precipitation Method", International Journal of Innovative Research in Science, Engineering and Technology, **5**(8), 15099 (2016). http://www.ijirset.com/upload/2016/august/60_15_Structural.pdf
[35] M.M. Rose, R.S. Christy, T.A. Benitta, and J.T.T. Kumaran, "Phase transitions in cadmium sulfide nanoparticles", AIP Advances **11**, 085129 (2021). https://doi.org/10.1063/5.0052078
[36] R.S. Christy, J.T.T. Kumaran, C. Bansal, and M. Brightson, "Phase transition in Cus-Ag_2S nanoparticle system", Phase Transition, **89**(2), 155 (2016). http://dx.doi.org/10.1080/01411594.2015.1102257
[37] M.M. Rose, R.S. Christy, T.A. Benitta, J.T.T. Kumaran, "Phase transitions in cadmium sulfide nanoparticles", AIP Advances, (2021). https://doi.org/10.1063/5.0052078
[38] R.R.A. Rozue, V. Shally, M.P. Dharshini, and S.G. Jayam, "Structural and Optical properties of Nickel Sulphide (NiS) nanoparticles", International Journal of Nano Science and Nanotechnology, **6**(1), 41 (2015). http://irphouse.com/ijnn/ijnnv6n1_05.pdf
[39] Y. Fazli, S.M. Pourmortazavi, I. Kohsari, M.S. Karimi, and M. Tajdari, "Synthesis, characterization and photocatalytic property of nickel sulfide nanoparticles", Journal of Materials Science: Materials in Electronics, **27**, 7192 (2016). https://doi.org/10.1007/s10854-016-4683-2

СТРУКТУРНІ, ЕЛЕКТРИЧНІ ТА ОПТИЧНІ ДОСЛІДЖЕННЯ СИСТЕМИ НАНОЧАСТИНОК $Ni_xCd_{1-x}S$ (x = 0,8, 0,6, 0,4 і 0,2)

Молі М. Роуз[a], Р. Шила Крісті[a], Т. Асенат Бенітта[a], Дж. Тампі Танка Кумаран[b]
[a]Департамент фізики та науково-дослідний центр (реєстр. № 18123112132030), Меморіальний християнський коледж Несамоні, Мартандам, філія університету Манонманіам Сундаранар, Абішекапатті, Тірунелвелі, Таміл Наду, Індія
[b]Відділ фізики та дослідницький центр Маланкарського католицького коледжу Маріагірі

У цій статті демонструється синтез наночастинок $Ni_xCd_{1-x}S$ (x = 0,8, 0,6, 0,4, 0,2) методом хімічного осадження за допомогою мікрохвиль. Підготовлені зразки охарактеризовані методами XRD, EDAX, SEM, UV-VIS та PL спектроскопії. Енергодисперсійний рентгенівський аналіз підтверджує існування нікелю, кадмію та сірки в належних співвідношеннях. Електричний опір постійному струму вимірювали в діапазоні температур 300 K-500 K. Криві температурного опору всіх зразків показують фазові переходи вище певної температури. УФ та ФЛ спектри всіх зразків були порівняні та досліджені.
Ключові слова: *наночастинки; хімічне осадження; фазовий перехід; електричні; оптичний; заборонена зона*

EAST EUROPEAN JOURNAL OF PHYSICS. **1.** 154-161 (2023)
DOI:10.26565/2312-4334-2023-1-19 ISSN 2312-4334

SYNTHESIS OF SnS/SnO NANOSTRUCTURE MATERIAL FOR PHOTOVOLTAIC APPLICATION†

Egwunyenga N. Josephine[a,b], Okunzuwa S. Ikponmwosa[b], Imosobomeh L. Ikhioya[c]*
[a]*Department of Science Laboratory Technology, Delta State Polytechnic, Ogwashi-Uku, Nigeria*
[b]*Department of Physics, University of Benin, Benin*
[c]*Department of Physics and Astronomy, University of Nigeria, Nsukka, 410001, Enugu State, Nigeria*
**Corresponding Author e-mail: imosobomeh.ikhioya@unn.edu.ng, nkeopene@gmail.com*
Received December 9, 2022; revised January 3, 2023; accepted January 16, 2023

Research Highlights:

- Successfully synthesized SnS/SnO nanostructured material using successors ionic layer absorption and reaction (SILAR) technique.
- Granular nanocrystals were visible in the materials, and they were strewn unevenly and randomly throughout the glass surface.
- It was found that the sample processed at room temperature had the largest energy band gap.
- The transmittance in the visible area of the spectrum was stable and SnS/SnO was at its maximum in the UV region

In this research, the SILAR method was used to synthesize environmentally-friendly SnS/SnO material for photovoltaic application, where 0.1 M of tin (II) chloride dihydrate ($SnCl_2.2H_2O$) was used to create the cationic precursor solution, and 0.01 M of thioacetamide (C_2H_5NS) was used to create the anionic precursor solution. The X-ray diffraction patterns of SnS/SnO material deposited on glass substrate at various deposition temperatures recorded a major peak at 45°C at 2 theta of 31.8997°, which corresponds to the face-centered cubic crystal structure (FCC). Diffraction peaks are visible in the pattern at planes 111, 200, 210, 211, and 300, which correspond to angles of 26.58°, 31.89°, 39.61°, 44.18°, and 54.85°, respectively. It was discovered that the crystallite/grain size and the lattice parameters decrease as the temperature of the deposition material rises. Granular nanocrystals were visible in the materials, and they were strewn unevenly and randomly throughout the glass surface. The spectra of the absorbance demonstrate that as light radiation passed through SnS/SnO films, it absorbed radiation as the wavelength increased from the UV region to the ultraviolet region of the spectra. It was discovered that the precursor temperature influences the material's absorbance; as the temperature rises, the absorbance decreases, making SnS/SnO an excellent material for photovoltaic systems. The transmittance in the visible area of the spectrum was stable and SnS/SnO was at its maximum in the UV region, it increased as the wavelength increased in the NIR region. It was found that the sample processed at room temperature had the largest energy band gap. SnS/SnO reveals an increase in thickness from 114.42 – 116.54 nm which resulted in a downturn in the resistivity of the deposited film from 9.040×10^{9} – 6.455×10^{9} (Ω·cm) while the conductivity of the deposited material increased from 1.106×10^{-10} – 1.549×10^{-10} $(\Omega\cdot cm)^{-1}$.

Keywords: *Tin sulphide; Nanocrystals; Nanostructure; EDX; XRD; SEM*
PACS: 72.80.Ey, 78.67.Bf, 62.23.St, 83.85.Hf, 78.70.Dm, 87.64.Dz

1. INTRODUCTION

Recently, there has been a lot of interest in the possible applications of semiconducting metal chalcogenide thin films in solid-state devices, such as photovoltaic, photoelectrochemical, photoconductive cells, solar cells, sensors, etc. The most interest has been shown in thin sulphide, a semiconducting metal chalcogenide with a high optical absorption coefficient and photoelectric conversion efficiency. An IV-VI semiconductor built of cheap, plentiful, and non-toxic SnS. It is possible to produce ecologically acceptable semiconductor materials for solar energy applications, such as tin sulphide and tin oxide, using the SILAR method. SnO_2 and SnS are important conversion materials because of their widespread natural occurrence, high theoretical gravimetric capacity, and environmental friendliness [1]. As a prospective window/buffer layer material for heterojunction solar cells, SnO_2 is considered one of the more recently approved transparent conducting oxides. However, it's an n-type semiconductor with a broad energy band gap of 3.8 eV and a higher molarity of free electrons than holes.

The SnS, on the other hand, is regarded as a more advantageous absorption layer material due to its high absorption coefficient, the p-type semiconductor band gap of 1.3 eV, and significantly higher hole concentration [2]. As a result, at the junction between the two semiconductors, holes diffuse from the SnS to the SnO2, as opposed to the SnO_2 in the case of the latter. Due to its high optical transparency (T>85% in the visible region), low electrical resistance, and good thermal resistance, tin oxide has primarily been used in a large number of optoelectronic devices, such as light-emitting diodes, buffer layer materials in solar cells, transparent filled effect transistors, etc. [3]. Tin oxide (SnO_2) is among the most important n-type semiconductors. The charge carriers annihilate at the intersection of these two diffusion modes, producing an internal electric field that accelerates the active movement of charges and ions and, as a result, results in high-rate capability [4]. SnS/SnO_2 heterostructures have a wide range of possible applications, from high-speed electronics to optoelectronics devices, because of their special interface features [5-7]. Because of the multiple heterojunction structures, the SnS/SnO_2 heterostructure exhibits significantly improved photocatalytic and photoelectrochemical performances. In addition, because SnS is more reversible than comparable oxides, it has a higher initial coulombic efficiency and reversible capacity [8-10].

† ***Cite as:*** E.N. Josephine, O.S. Ikponmwosa, and I.L. Ikhioya, East Eur. J. Phys. **1**, 154 (2023), https://doi.org/10.26565/2312-4334-2023-1-19

Sugiyama et al., who created a typical SnS-based solar cell with a glass/SnO_2/SnS/CdS/ZnO configuration, claim that they measured band discontinuities at SnO_2/SnS heterointerfaces using X-ray photoelectron spectroscopy and found that SnO_2/SnS interfaces produced evaluated valence band offsets of about 3.5 eV [11]. El-Etre and Red (2010) [12] created a nanocrystalline SnO_2 thin film using cathodic electrodeposition-anodic oxidation and then used X-ray diffraction, SEM, UV-visible absorption, and nitrogen adsorption-desorption by BET technique to determine the structure of the film. The final film has a grain size of 24 nm and a surface area of 137.9 m^2/g. In dye-sensitized solar cells, the produced SnO_2 thin film can therefore be used as an electrode. Tin oxide (SnO_2), one of many metal oxides, has drawn a lot of attention as a viable candidate material due to its myriad uses. SnO_2 is widely utilized for a variety of high-tech applications, including dye-sensitized solar cells, gas sensors, photocatalysts, lithium-ion batteries, and supercapacitors, to mention a few [13]. These applications include optical and electrical qualities, high chemical stability, and theoretical capacity.

The films can be created using several techniques, such as spray pyrolysis, electrode placement, chemical bath deposition (CBD), vacuum evaporation, SILAR, etc. SILAR is the most straightforward, affordable, and quickly implemented method available [14-17]. Broad surfaces can be covered with thin films using SILAR, and the thickness can be changed by adjusting the number of dippings.

In this research, the successor's ionic layer absorption and reaction (SILAR) technique were used to synthesize environmentally-friendly SnS/SnO material for photovoltaic application, were 0.1 M of tin (II) chloride dihydrate ($SnCl_2{\cdot}2H_2O$) was used to create the cationic precursor solution, and 0.01 M of thioacetamide (C_2H_5NS) was used to create the anionic precursor solution. The film will be characterized for their Phase identification by X-ray diffraction and scanning electron microscope (SEM) model A-VPSE G3 was used to determine the chemical compositions of the thin films produced in this work.

2. EXPERIMENTAL PROCEDURE

The following precursors were employed in the deposition of SnS/SnO: 0.1 M of tin (II) chloride dihydrate ($SnCl_2.2H_2O$) was used to create the cationic precursor solution, and 0.01 M of thioacetamide (C_2H_5NS) was used to create the anionic precursor solution. Four sets of 50 ml beakers containing tin (II) chloride dihydrate ($SnCl_2{\cdot}2H_2O$) solution. Distilled water, and Thioacetamide (C_2H_5NS)/potassium hydroxide (KOH) solution. A well-cleaned glass substrate that had been washed with acetone, distilled water, and acid was submerged in a cationic precursor solution of tin (II) chloride dihydrate ($SnCl_2{\cdot}2H_2O$) for 10 seconds to allow tin ions to adhere to the surface of the substrate. To get rid of the loosely attached Sn^{2+} ions, the substrate was washed in distilled water for 5 seconds. The substrate was then submerged in the Thioacetamide (C_2H_5NS)/potassium hydroxide (KOH) anionic precursor solution for 10 seconds to create a layer of SnS/SnO materials. One SILAR cycle of SnS deposition was finished by rinsing the substrate once more in distilled water for 5 s to remove the unreached species. Such cycles were repeated for various variations at various temperatures. The precursor pH was kept constant at 7.0 while all other parameters, including the deposition temperature, varied between 50ºC, 55ºC, 60ºC, and 65ºC during the synthesis. Tin sulphide (SnS) was next deposited on the developed SnO films to create SnS/SnO superlattice films, and the process was repeated for a different parameter for characterization. Tin oxide (SnO) was initially coated on the glass substrate dry in the oven for 30 minutes.

2.1. Characterization Techniques

The characterization of the deposited films was ascertained using some currently in-use techniques. Knowing the chemical composition, crystal structure, crystallite size, surface morphology, band gap energy, optical absorption, transmittance, and absorbance of the formed film is possible thanks to characterization. Phase identification of the films by X-ray diffraction was used to determine the chemical compositions of the thin films produced in this work using a scanning electron microscope (SEM) model A-VPSE G3 with an acceleration voltage of 20 kV and a magnification range of 200x to 1000x, the morphology and size of the prepared particles were investigated. The optical characteristics of the films deposited were examined for their absorbance and transmittance at normal incidence by using a UV-visible spectrophotometer, model number 756S.

3. RESULTS AND DISCUSSIONS

Figure 1 displays the X-ray diffraction patterns of SnS/SnO material deposited on a glass substrate at various temperatures. The major peak was discovered at 45ºC at 2 theta of 31.8997º, which corresponds to the face-centered cubic crystal structure (FCC). SnS/SnO was recognized as the orientations along the (200) plane and the (300), respectively. It was stated that the lattice constant was $\alpha = 5.8028$ Å. Several peaks were found to support the usage of SnS/SnO material as a hole transport material in solar cells and photovoltaic systems. The SILAR method was used to deposit this material. The Debye-Scherrer equation was used to calculate the average crystallite sizes based on the diffraction peaks' full width at half maximums (FWHM). The polycrystalline nature of the films was revealed by the XRD pattern. Diffraction peaks are visible in the pattern at planes 111, 200, 210, 211, and 300, which correspond to angles of 26.58°, 31.89°, 39.61°, 44.18°, and 54.85°, respectively. The unindexed peaks could have been brought on by the glass substrates used for the deposition. Table 1 displays the calculated structural characteristics of the material. It was discovered that the crystallite/grain size and the lattice parameters decrease as the temperature of the deposition material rises. This size reduction would increase the crystallinity of the deposited films and increase the efficiency of photon absorption.

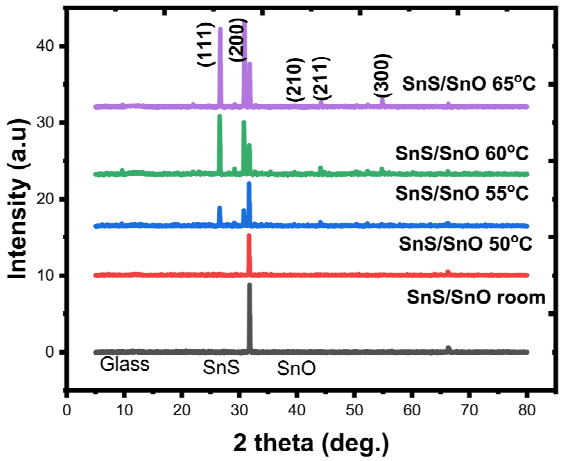

Figure 1. XRD pattern of SnS/SnO material

Table 1. Structural values for the SnS/SnO

Films	2θ (degree)	Spacing d(Å)	Lattice constant (Å)	FWH, β	Hkl	Crystallite Size, D (nm)	Dislocation density, δ m^2
SnS/SnO room	26.5815	3.3502	5.8028	0.1851	111	0.7694	5.1218
SnS/SnO 50°C	31.8997	2.8028	5.6056	0.2095	200	0.6880	6.4151
SnS/SnO 55°C	39.6196	2.2726	5.5453	0.1480	210	0.6957	6.0633
SnS/SnO 60°C	44.1829	2.0479	4.5793	0.2258	211	0.7626	6.8539
SnS/SnO 65°C	54.8536	1.6721	4.0958	0.2249	300	0.7543	6.2663

3.1. SEM Micrograph of SnS/SnO Material

The surface micrograph of SnS/SnO material deposited at various precursor temperatures (45°C-65°C) is shown in Figure 2.

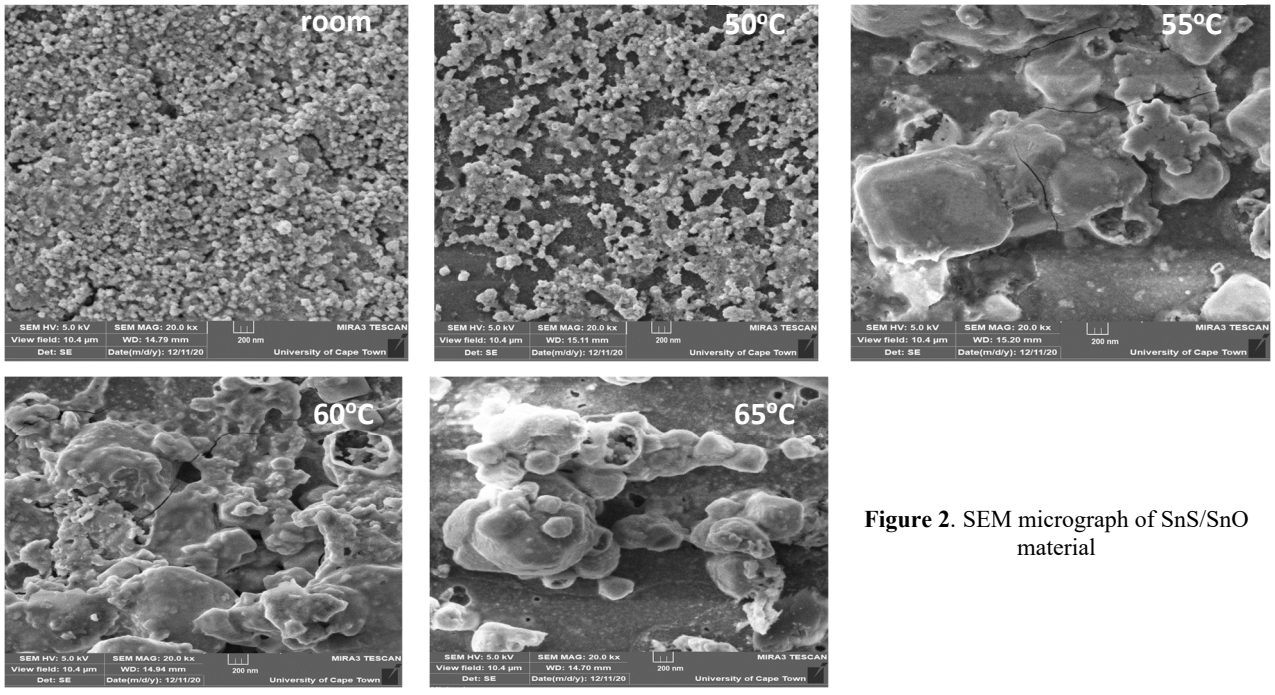

Figure 2. SEM micrograph of SnS/SnO material

All of the deposited materials' surface morphological images were scanned at a magnification of 200 nm. Granular nanocrystals were visible in the materials, and they were strewn unevenly and randomly throughout the glass surface. In contrast to SnS/SnO deposited at 50°C, which has a similar image but shows the particle is scattered on the glass surface, the SnS/SnO image at room temperature shows sand-like particles well packed together without pinholes, while the material is deposited between 55 and 65 degrees Celsius, the nano grain is larger than when it is placed at 50 degrees. The material left behind demonstrates how the growth of big grains led to the agglomeration of the particles. The films' increasing grain sizes demonstrate that as the precursor temperature rises, the size of the crystallites also grows, providing more room for light absorption and trapping following penetration. This property makes the deposited films potential

photovoltaic materials. The elemental constituents of SnS/SnO material showed in Figure 3. The position of the peaks in a typical EDX spectrum confirms the presence of the fundamental elements, and the peak height helps quantify each element's concentration in the film samples. The material's EDX results show that tin, sulfur, and oxygen are present, with a greater intensity peak for tin and oxygen and proof of sulfur's presence. The constituent elements of the glass substrate used for the deposition were created as a result of the other element on the spectrum.

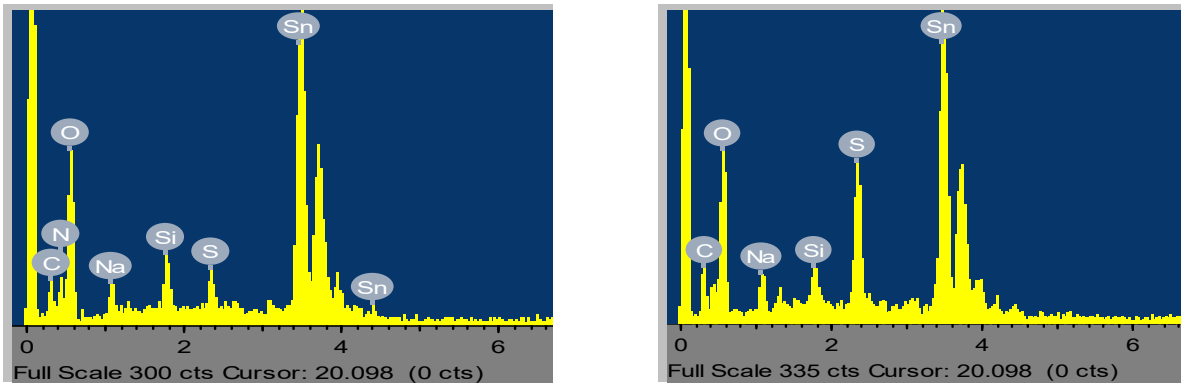

Figure 3. EDX spectra

3.2. The optical study

The SnS/SnO was investigated for their optical examination to determine how quickly it absorbed light. According to Figure 4(“a”), the spectra of the absorbance demonstrate that as light radiation passed through SnS/SnO films, it absorbed radiation as the wavelength increased from the UV region to the ultraviolet region of the spectra. The absorbance also slightly decreased along the NIR infrared region as the wavelength increased.

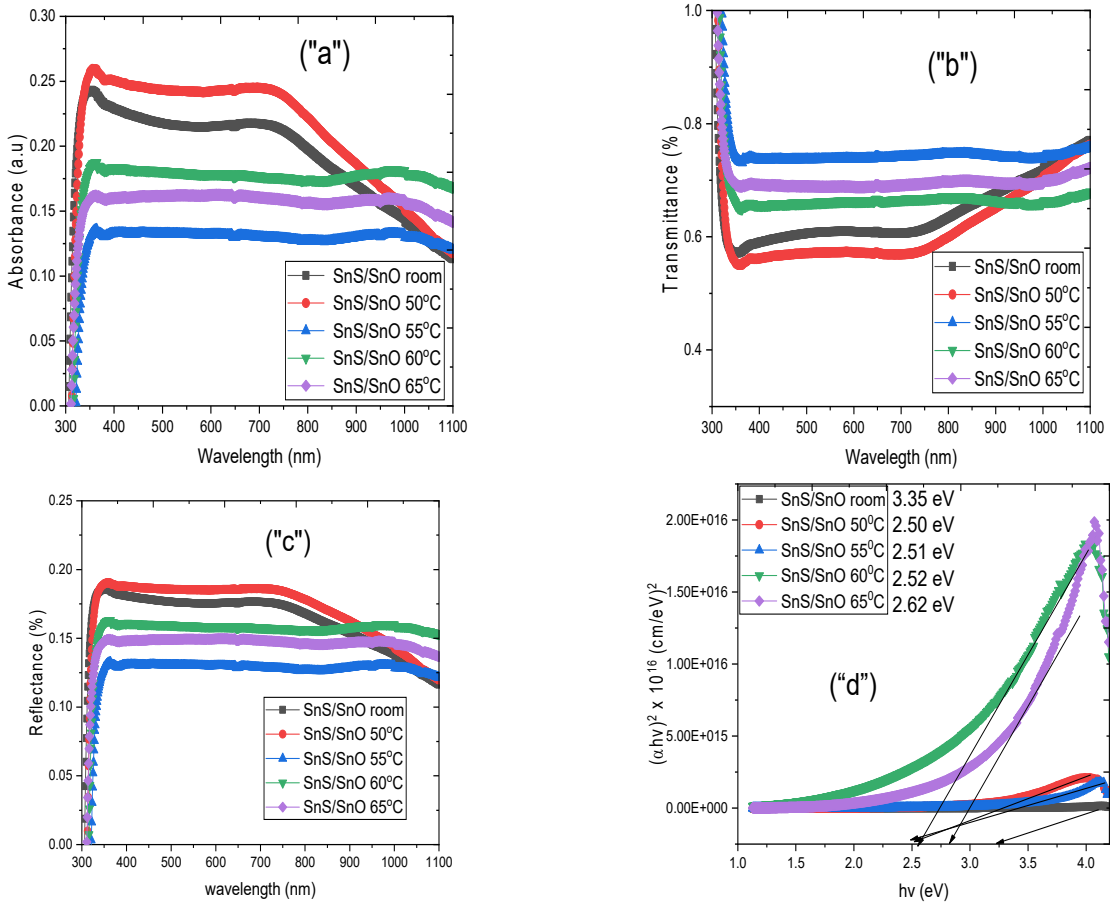

Figure 4. (“a”) absorbance, (“b”) transmittance, (“c”) reflectance, and (“d”) band gap energy

It was discovered that the precursor temperature influences the material's absorbance; as the temperature rises, the absorbance decreases, making SnS/SnO an excellent material for photovoltaic systems. Figure 4(“b”) depicts the SnS/SnO material's transmittance. While the transmittance in the visible area of the spectrum was stable and SnS/SnO was at its maximum in the UV region, it increased as the wavelength increased in the NIR region. The transmittance was also

impacted by temperature, which led to an increase in SnS/SnO transmittance in the UV and ultraviolet parts of the spectrum. From Figure 4("c"), the reflectance decreases as wavelength increases. The reflectance is moderate at the visible region. It also shows that the reflectance reduces, with an increase in the temperature of the precursor. The energy band gap spectra of the deposited SnS/SnO films are depicted in Figure 4 ("d") and were estimated using the Tauc equation: $(\alpha h\upsilon)^{1/n} = \beta(h\upsilon - E_g)$. 3.35 eV is the band gap determined from the film at ambient temperature. It was found that the sample processed at room temperature had the largest energy band gap. 2.50 eV, 2.51 eV, 2.52 eV, and 2.62 eV are the calculated energy band gap values.

The extinction coefficient of the SnS/SnO material is plotted in Figure 5 ("a"). The extinction coefficient gradually rises as the spectra's energy level approaches. It also showed how the precursor temperature affected the films. Using equation 1, the reflectance data were used to estimate the refractive index is shown in Figure 5 ("b")

$$\boldsymbol{n = \frac{1+R}{1-R} + \sqrt{\frac{4R}{(1-R)^2} - K^2}.} \quad (1)$$

The non-linear refractive index pattern suggests a change in the samples' typical dispersion characteristics. This demonstrates how the refractive index is independent of wavelength. Higher deposition temperatures caused the visible part of the electromagnetic spectrum, where it ends at a value of 1.11, to have narrower spectra. The sample that was deposited at 60°C had a wider spectrum, while the sample that was deposited at 65°C was second. The sample deposited at 70°C had a wider spectrum than the sample deposited at 50°C in terms of the sequence. The sample deposited at 55°C has the narrowest spectrum. Electrical transport at high optical frequencies is related to quantitative measurements in Figure 5 ("c") optical conductivity. The optical conductivity spectra of a material are frequently used to describe its response to light. Its dimensions are measured in units per second (S^{-1}), which are equivalent to the frequency in the Gaussian unit. A progressive climb towards higher energy levels is followed by a decrease in the optical conductivity of the SnS/SnO material.

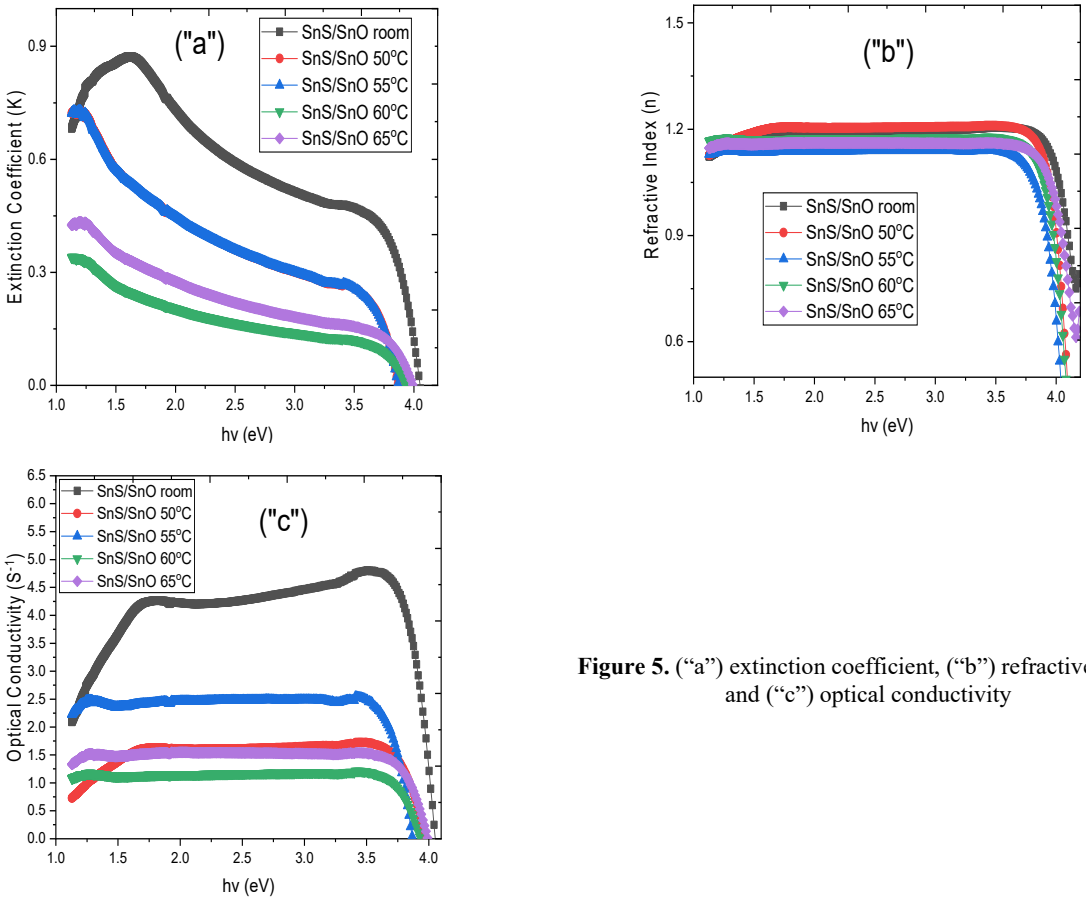

Figure 5. ("a") extinction coefficient, ("b") refractive index, and ("c") optical conductivity

Figures 6 ("a") and ("b") demonstrate the dielectric constant of SnS/SnO; the former indicates energy loss; the latter indicates how effectively dielectric materials store electrical energy. Permittivity in alternating current fields includes both real and fictitious components that, respectively, represent dielectric losses and polarization levels. Furthermore, affected by frequency is the dielectric constant. The spectra of the real and imaginary dielectric constants of the deposited SnS/SnO showed that the real and imaginary dielectric constant values increased with the photon energy of the material. This demonstrates that the deposited materials become helpful for solar systems when their temperature is raised.

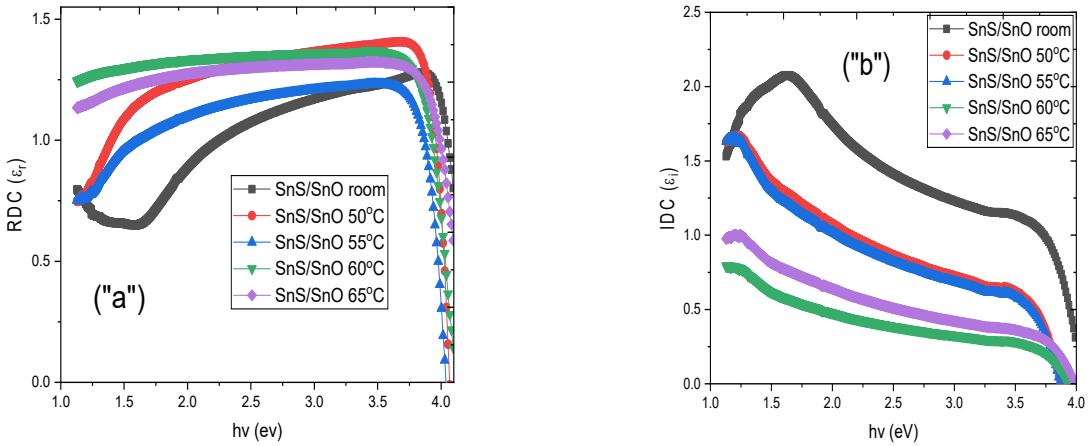

Figure 6. ("a") real, and ("b") imaginary dielectric constant

The material deposited at different temperatures reveals an increase in thickness from 114.42 – 116.54 nm which resulted in a downturn in the resistivity of the deposited film from 9.040×10^{9} – 6.455×10^{9} (Ω.cm) while the conductivity of the deposited material increased from 1.106×10^{-10} - 1.549×10^{-10} $(\Omega\cdot cm)^{-1}$. Figure 7 ("a") and ("b") show the plot of resistivity and conductivity against thickness and precursor temperature, from the plot increase in thickness, resulted in an increase in conductivity and a decrease in resistivity and an increase in precursor temperature beginning about the increase in conductivity and decrease in resistivity. The deposited material will be a good candidate for photovoltaic and solar cell applications.

Table 2. Electrical properties of SnS/SnO

Films	Thickness, t (nm)	Resistivity, **ρ** (Ω.cm)×10^{9}	Conductivity, **σ** (S/m)×10^{-10}
SnS/SnO room	114.42	9.040	1.106
SnS/SnO 50°C	115.32	8.237	1.214
SnS/SnO 55°C	115.42	7.643	1.308
SnS/SnO 60°C	116.33	7.431	1.345
SnS/SnO 65°C	116.54	6.455	1.549

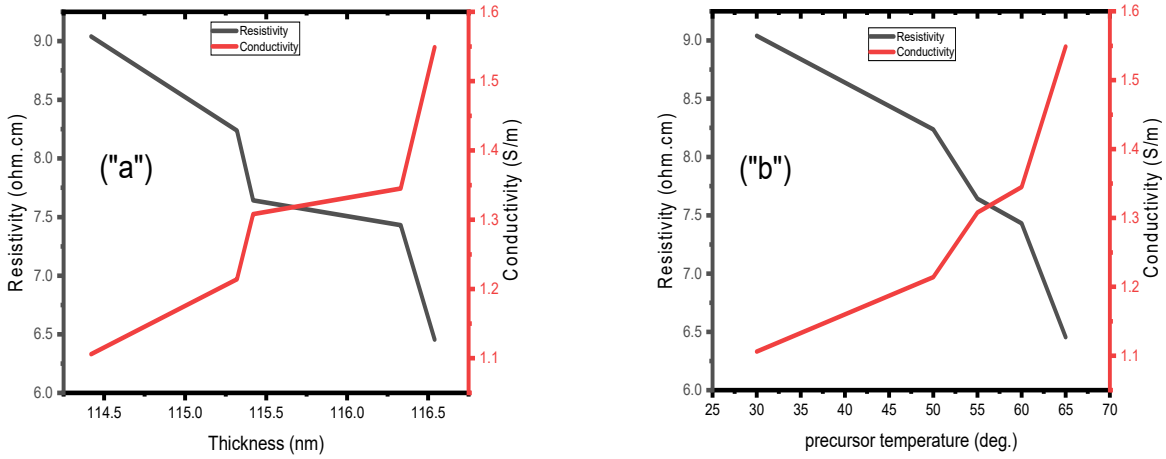

Figure 7. ("a") plot of resistivity and conductivity against thickness and ("b") precursor temperature

4. CONCLUSION

SnS/SnO material has been successfully deposited using the SILAR method. The X-ray diffraction patterns of SnS/SnO material deposited on glass substrate at various deposition temperatures recorded a major peak at 45°C at 2 theta of 31.8997°, which corresponds to the face-centered cubic crystal structure (FCC). SnS/SnO was recognized as the orientations along the (200) plane and the (300), respectively. It was stated that the lattice constant was $\alpha = 5.8028$ Å. Several peaks were found to support the usage of SnS/SnO material as a hole transport material in solar cells and photovoltaic systems. The polycrystalline nature of the films was revealed by the XRD pattern. Diffraction peaks are visible in the pattern at planes 111, 200, 210, 211, and 300, which correspond to angles of 26.58°, 31.89°, 39.61°, 44.18°,

and 54.85°, respectively. It was discovered that the crystallite/grain size and the lattice parameters decrease as the temperature of the deposition material rises. This size reduction would increase the crystallinity of the deposited films and increase the efficiency of photon absorption. All of the deposited materials' surface morphological images were scanned at a magnification of 200 nm. Granular nanocrystals were visible in the materials, and they were strewn unevenly and randomly throughout the glass surface. In contrast to SnS/SnO deposited at 50ºC, which has a similar image but shows the particle is scattered on the glass surface, the SnS/SnO image at room temperature shows sand-like particles well packed together without pin holes. the spectra of the absorbance demonstrate that as light radiation passed through SnS/SnO films, it absorbed radiation as the wavelength increased from the UV region to the ultraviolet region of the spectra. The absorbance also slightly decreased along the NIR infrared region as the wavelength increased. It was discovered that the precursor temperature influences the material's absorbance; as the temperature rises, the absorbance decreases, making SnS/SnO an excellent material for photovoltaic systems. The transmittance in the visible area of the spectrum was stable and SnS/SnO was at its maximum in the UV region, it increased as the wavelength increased in the NIR region. The transmittance was also impacted by temperature, which led to an increase in SnS/SnO transmittance in the UV and ultraviolet parts of the spectrum. The energy band gap spectra of the deposited SnS/SnO films were determined from the film at ambient temperature. It was found that the sample processed at room temperature had the largest energy band gap. SnS/SnO reveals an increase in thickness from 114.42– 116.54 nm which resulted in a downturn in the resistivity of the deposited film from 9.040×10^{9} – 6.455×10^{9} (Ω·cm) while the conductivity of the deposited material increased from 1.106×10^{-10} - 1.549×10^{-10} $(\Omega\cdot cm)^{-1}$.

Acknowledgment

The research was funded by Tetfund Institution Based Research (IBR), which the authors acknowledge.

ORCID IDs

Imosobomeh L. Ikhioya, https://orcid.org/0000-0002-5959-4427

REFERENCE

[1] B. Zhao, H. Zhuang, Y. Yang, Y. Wang, H. Tao, Z. Wang, and Y. Jiang, "Composition-dependent lithium storage performances of SnS/SnO_2 heterostructures sandwiching between spherical graphene", Electrochimica Acta, **300**, 253-262 (2019). https://doi.org/10.1016/j.electacta.2019.01.116

[2] Y. Akaltun, A. Astam, A. Cerhan and T. Çayir, "Effects of thicknes on electrical properties of SILAR deposited SnS thin films", AIP Conference Proceedings, **1722**, 220001 (2016). https://doi.org/10.1063/1.4944233

[3] Z. Chen, D. Yin, and M. Zhang, "Sandwich-like MoS2@ SnO2@ C with high capacity and stability for Sodium/Potassium ion batteries", Small, **14**, 1703818 (2018). https://doi.org/10.1002/smll.201703818

[4] Y. Zheng, T. Zhou, C. Zhang, J. Mao, H. Liu, and Z. Guo, "Boosted charge transfer in SnS/SnO2 heterostructures: toward high rate capability for sodium-ion batteries", Angewandte Chemie, **128**(10), 3469-3474 (2016). https://doi.org/10.1002/ange.201510978

[5] X. Zhu, N.R. Monahan, Z. Gong, H. Zhu, K.W. Williams, and C.A. Nelson, "Charge transfer excitons at van der Waals interfaces", Journal of the American Chemical Society, **137**(26), 8313-8320 (2015). https://doi.org/10.1021/jacs.5b03141

[6] P. Zubko, S. Gariglio, M. Gabay, P. Ghosez, and J.M. Triscone, "Interface physics in complex oxide heterostructures", Annu. Rev. Condens. Matter Phys. **2**(1), 141-165 (2011). https://doi.org/10.1146/annurev-conmatphys-062910-140445

[7] C. Huang, S. Wu, A.M. Sanchez, J.J. Peters, R. Beanland, J.S. Ross, P. Rivera, W. Yao, D.H. Cobden, and X. Xu, "Lateral heterojunctions within monolayer $MoSe_2$–WSe_2 semiconductors", Nature materials, **13**(12), 1096-1101 (2014). https://doi.org/10.1038/nmat4064

[8] D.Y. Yu, P.V. Prikhodchenko, C.W. Mason, S.K. Batabyal, J. Gun, S. Sladkevich, A.G. Medvedev, and O. Lev, "High-capacity antimony sulphide nanoparticle-decorated graphene composite as anode for sodium-ion batteries", Nature communications, **4**(1), 1-7 (2013). https://doi.org/10.1038/ncomms3922

[9] C. Bommier, and X. Ji, "Recent development on anodes for Na-ion batteries", Israel Journal of Chemistry, **55**(5), 486-507 (2015). https://doi.org/10.1002/ijch.201400118

[10] H. Bian, Z. Li, X. Xiao, P. Schmuki, J. Lu, and Y.Y. Li, "Tunable transformation between SnS and SnOx nanostructures via facile anodization and their photoelectrochemical and photocatalytic performance", Solar RRL, **2**(11), 1800161 (2018). https://doi.org/10.1002/solr.201800161

[11] M. Sugiyama, Y. Murata, T. Shimizu, K. Ramya, C. Venkataiah, T. Sato, and K.R. Reddy, "Sulfurization growth of SnS thin films and experimental determination of valence band discontinuity for SnS-related solar cells", Japanese Journal of Applied Physics, **50**(5S2), 05FH03 (2011). https://doi.org/10.1143/JJAP.50.05FH03

[12] A.Y. El-Etre, and S.M. Reda, "Characterization of nanocrystalline SnO_2 thin film fabricated by electrodeposition method for dye-sensitized solar cell application", Applied Surface Science, **256**(22), 6601-6606 (2010). https://doi.org/10.1016/j.apsusc.2010.04.055

[13] B. Yuliarto, N. Nugraha, B. Epindonta, R. Aditia, and M. Iqbal, "Synthesis of SnO_2 Nanostructure Thin Film and its Prospective as Gas Sensors", Advanced Materials Research, **789**, 189–92 (2015). https://doi.org/10.4028/www.scientific.net/AMR.789.189

[14] K. Jain, R.P. Pant, and S.T. Lakshmikumar, "Effect of Ni doping on thick film SnO_2 gas sensor", Sens. Actuators B, **113**, 823 (2006). https://doi.org/10.1016/j.snb.2005.03.104

[15] Li X., Gao C., Duan H., Lu B., Wang Y., Chen L., Zhang Z., Pan X. and L.E. Xie, "High-performance photoelectrochemical - typeself powered UV photodetector using epitaxial TiO_2/SnO_2 branched heterojunction nanostructure", Small, **9**, 2005 (2013). https://doi.org/10.1002/smll.201202408

[16] W. Tian, T. Zhai, C. Zhang, S.-L. Li, X. Wang, F. Liu, D. Liu, et al, "Low-cost fully transparent ultraviolet photodetectors based on electrospun ZnO-SnO_2 heterojunction nanofibers", Adv. Mater. **25**, 4625–30 (2013). https://doi.org/10.1002/adma.201301828
[17] Q. Jiang, X. Zhang, and J. You, "SnO_2: a wonderful electron transport layer for perovskite Solar Cells", Small, **14**, 1801154 (2018). https://doi.org/10.1002/smll.201801154

СИНТЕЗ НАНОСТРУКТУРНОГО МАТЕРІАЛУ SnS/SnO ДЛЯ ФОТОЕЛЕКТРИЧНОГО ЗАСТОСУВАННЯ

Егвуньєнга Н. Джозефін[a,b], Окунзува С. Ікпонмвоса[b], Імособоме Л. Іхіоя[c]
[a]Відділ наукових лабораторних технологій, Delta State Polytechnic, Ogwashi-Uku, Нігерія
[b]Фізичний факультет, Університет Беніну, Бенін
[c]Факультет фізики та астрономії, Університет Нігерії, Нсукка, 410001, штат Енугу, Нігерія

Основні моменти дослідження:

• Успішно синтезовано наноструктурний матеріал SnS/SnO з використанням наступної техніки поглинання та реакції іонного шару (SILAR).

• У матеріалах було видно зернисті нанокристали, які були нерівномірно та хаотично розкидані по всій поверхні скла.

• Було виявлено, що зразок, оброблений при кімнатній температурі, мав найбільшу заборонену зону.

• Коефіцієнт пропускання у видимій частині спектру був стабільним, а SnS/SnO був максимальним в УФ-області

У цьому дослідженні метод SILAR використовувався для синтезу екологічно чистого матеріалу SnS/SnO для фотоелектричного застосування, де 0,1 М дигідрату хлориду олова (II) ($SnCl_2 \cdot 2H_2O$) використовувалося для створення розчину катіонного прекурсора, а 0,01 М тіоацетамід (C_2H_5NS) використовували для створення розчину аніонного прекурсора. Рентгенівські дифрактограми матеріалу SnS/SnO, нанесеного на скляну підкладку при різних температурах осадження, зафіксували основний пік при 45°C при 2 тета 31,8997°, що відповідає гранецентрованій кубічній кристалічній структурі (FCC). На картині видно дифракційні піки в площинах 111, 200, 210, 211 і 300, які відповідають кутам 26,58°, 31,89°, 39,61°, 44,18° і 54,85° відповідно. Було виявлено, що розмір кристалітів/зерен і параметри решітки зменшуються з підвищенням температури матеріалу осадження. У матеріалах було видно зернисті нанокристали, які були нерівномірно та безладно розкидані по всій поверхні скла. Спектри поглинання демонструють, що коли світлове випромінювання проходило через плівки SnS/SnO, воно поглинало випромінювання, коли довжина хвилі зростала від УФ-області до ультрафіолетової області спектру. Було виявлено, що температура прекурсора впливає на поглинання матеріалу; у міру підвищення температури абсорбція зменшується, що робить SnS/SnO чудовим матеріалом для фотоелектричних систем. Коефіцієнт пропускання у видимій області спектру був стабільним, а SnS/SnO був максимальним в УФ-діапазоні, він зростав зі збільшенням довжини хвилі в ближньому ІЧ-діапазоні. Було виявлено, що зразок, оброблений при кімнатній температурі, мав найбільшу заборонену зону. SnS/SnO виявляє збільшення товщини від 114,42 до 116,54 нм, що призвело до зниження питомого опору осадженої плівки з $9{,}040\times10^{9}$ (Ω·см) до $6{,}455\times10^{9}$ (Ω·см), тоді як провідність осадженого матеріалу зросла з $1{,}106\times10^{-10}$ $(\Omega\cdot см)^{-1}$ до $1{,}549\times10^{-10}$ $(\Omega\cdot см)^{-1}$.

Ключове слово: *сульфід олова; нанокристали, наноструктура; EDX; XRD; SEM*